UNIVERSITY OF CALIFORNIA
SANTA CRUZ

ACTIVE GALACTIC NUCLEI AND MERGING GALAXIES, OR THE CAUSE AND EFFECT OF BLACK HOLE GROWTH AT $Z \sim 1$

A dissertation submitted in partial satisfaction of the
requirements for the degree of

DOCTOR OF PHILOSOPHY

in

PHYSICS

by

Christina M. Pierce

March 2009

The Dissertation of Christina M. Pierce
is approved:

Professor Joel R. Primack, Chair

Professor Sandra M. Faber

Professor David C. Koo

Doctor Jennifer M. Lotz

Lisa C. Sloan
Vice Provost and Dean of Graduate Studies

Table of Contents

List of Figures

List of Tables

Abstract

Active Galactic Nuclei and Merging Galaxies, or

the Cause and Effect of Black Hole Growth at $z \sim 1$

by

Christina M. Pierce

This thesis investigates the causes and effects of AGNs by studying the color and morphology characteristics of their host galaxies. AGNs were selected based on their X-ray luminosities, radio powers, and/or optical spectra signatures. Extensive multiwavelength data from two complementary surveys, the All-wavelength Extended Groth Strip Interational Survey (AEGIS) and the northern field of the Great Observatories Origins Deep Survey (GOODS-N) were used to select AGNs and corresponding control samples. It was found that AGN host galaxies are more likely than galaxies in the corresponding control samples to be morphologically classified as interacting, early-type, bulge-dominated, and/or E/S0/Sa, suggesting that they are currently interacting or may have undergone a merger in the recent past. AGN hosts were *not* more likely to have a close kinematic companion, potentially restricting the intial start of significant nuclear activity to well into interaction. Simulations used to test the reliability of the color and morphology measurements used here indicate that the measurements are potentially sensitive to low-luminosity contributions from AGNs, but that the AGN should also become visible as an optical point source at these low luminosities, and so would be identifiable as a potential source of contamination.

Chapter 1

Introduction

1.1 Review of relevant background

Numerous authors have described a strongly bimodal distribution among the rest-frame colors of galaxies out to redshifts of at least $z \sim 1$ (e.g., Bell et al. 2004b; Strateva et al. 2001; Baldry et al. 2004; Balogh et al. 2004; Weiner et al. 2005; Cirasuolo et al. 2007). This distribution separates galaxies into a "red sequence" and a "blue cloud", so named because of the relatively smaller spread in the colors of red galaxies as compared to the spread in the colors of blue galaxies (see, e.g., Baldry et al. 2004, Figure 1). It has further been found that the optical colors of a galaxy correlate well with its morphological characteristics. The red sequence, especially at redshifts $z < 0.7$, consists mainly of spheroidal or spheroid-dominated galaxies that are typically experiencing minimal star formation, if any, while the star-forming galaxies populating the blue cloud generally have later Hubble types (e.g., de Vaucouleurs 1961; Blanton et al. 2003;

Bell et al. 2004b; Weiner et al. 2005; Scarlata et al. 2007b).

Baldry et al. (2004) found that the red and blue peaks of the $u-r$ optical color bimodality are well fitted by a pair of Gaussians, and their work clearly showed a lack of galaxies with colors between the two peaks (see their Figures 3 and 4), often referred to as the "green valley" and representing a probable transition region. In contrast, Wyder et al. (2007) found that the $NUV-r$ UV-optical colors revealed a substantially more heavily populated green valley. Their Figures 12-14 show that the UV-optical red and blue peaks are still well fitted by Gaussians, but the number of galaxies with colors falling *between* the two peaks significantly exceeds the sum of the Gaussians. In spite of the differences between the number of galaxies populating the green valley, both the optical colors and the UV-optical colors exhibit significant red-blue bimodalities. Furthermore, the number of green valley galaxies is less than would be expected from normal aging of the stellar population following a shut-down of star formation that had been caused exclusively by gas exhaustion. In addition, it has recently been discovered that the current ($z = 0$) total mass of red sequence galaxies is a factor of 3 higher than it was at $z = 1$ (Bell et al. 2004a; Faber et al. 2007; Brown et al. 2007).

The relatively empty green valley and the significant growth of the red sequence may result from internal and/or external influences that have the ability to cause blue, star-forming, disk galaxies to transition rapidly to red spheroid-dominated systems. Possible explanations for the rapid growth of the red sequence, as well as the dearth of galaxies populating the green valley, include mergers between gas-rich and gas-poor galaxies (Mihos & Hernquist 1996; Bell et al. 2004b, 2006a,b; Blanton 2006), virial

shock heating of the gas (Birnboim et al. 2007), galaxy harassment (Moore et al. 1998), and various kinds of feedback from an active galactic nucleus (AGN; e.g., Hopkins et al. 2008a,b; Cox et al. 2006; Springel et al. 2005; Di Matteo et al. 2005; Croton et al. 2006). Three important results offer a measure of support for scenarios in which galaxy interactions and/or AGN feedback provide the sought after influence to rapidly drive galaxies from the blue cloud to the red sequence and to increase the mass of red sequence galaxies roughly threefold between $z = 1$ and the present.

First of all, for many years, observations have been providing evidence that spheroids consistently contain supermassive black holes, the masses of which scale with both the mass ($M_{\rm BH} \sim 10^{-4} M_{\rm sph}$) and the stellar velocity dispersion of the spheroid, though the correlation is much tighter with the latter (e.g., Kormendy & Richstone 1995; Magorrian et al. 1998; Ferrarese & Merritt 2000; Gebhardt et al. 2000). Together these indicate a strong relationship between the growth of a supermassive black hole and the growth of the spheroid in which it resides – either the black hole affects the growth of the stellar spheroid, or vice versa.

Secondly, although the majority of morphologically classified AGN host galaxies have been determined to be early-type or spheroid-dominated (e.g., Grogin et al. 2003, 2005; Pierce et al. 2007), a number of authors have reported spheroid-dominated systems that are observed to have morphological evidence of a recent interaction (e.g., Schweizer et al. 1990; van Dokkum 2005), and this may be particularly true for spheroidal systems that host an AGN (e.g., Bennert et al. 2008; Urrutia et al. 2008).

Finally, many of the researchers who have completed simulations and semi-

analytic models of galaxy interactions and evolution have included supermassive black holes at the centers of the initial galaxies (e.g., Kauffmann & Haenelt 2000; Croton et al. 2006; Ciotti & Ostriker 2007; Hopkins et al. 2005a,b, 2008a,b; Somerville et al. 2008), and they invariably find that the black holes become active during some stage of a merger event between gas-rich galaxies of similar masses (a "major merger", typically defined as a merger between galaxies having a mass ratio between 1:1 and 1:3). Most of these authors found that some form of radiative output (or "feedback") from the AGN significantly decreased the star formation rate in the galaxy, although the methods by which this happened differ. For example, Hopkins et al. (2005a,b, 2008a,b) described a form of AGN feedback that forcefully removes gas from the nuclear regions of a galaxy, after significant star formation and accretion onto the black hole has used up much of the gas. Croton et al. (2006) presented an alternative scenario, a "radio mode", in which AGN feedback heats the nuclear gas to temperatures sufficient to shut down star formation, without necessarily removing the gas from the galaxy.

Both forms of feedback significantly decrease the growth of both the black hole and the stellar spheroid, potentially moving the galaxy through the green valley more rapidly than should be expected if the nucleus was not active. Some observational support for the scenarios derived from the simulations and semi-analytic models has recently been provided by Schawinski et al. (2007) and Georgakakis et al. (2008).

After visually examining $\sim$16,000 low-redshift early-type galaxies and spectroscopically classifying each as experiencing star formation, black hole growth, a combination of the two, or neither, Schawinski et al. (2007) presented evidence that radiative

output from an AGN may cause its host galaxy to transition from a star-forming system to a quiescent system. Approximately 20% of their galaxies were detected to have emission lines (placing them into one of the first three categories listed above), and Schawinski et al. found that the optical colors of these systems were typically bluer than the quiescent systems, and that the magnitude of the offset from the red sequence depended on the type of activity observed.

Most of the systems dominated by emission from low-ionization nuclear emission line regions (LINERs) joined the inactive galaxies populating the red sequence, while the remaining LINER hosts and the Seyfert hosts typically had colors on the red edge of the green valley. Early-type systems undergoing star formation were found in the blue cloud, and the systems exhibiting emission lines characteristic of both an AGN *and* star formation typically populated the green valley. After also considering the star formation histories of the four galaxy samples, they concluded that the AGN must contribute to the observed decrease in star formation among low- and intermediate-mass early-type galaxies; they also suggested that the AGNs in high-mass galaxies may almost entirely prevent star formation. Both of their conclusions seem to support the idea that AGN feedback negatively influences the star formation rates of the host galaxies.

Georgakakis et al. (2008) stacked the X-ray emissions of three samples of galaxies at $z \sim 0.7$; the samples were comprised of galaxies with optical colors placing them on the red sequence, the green valley, or the blue cloud. After stacking, they found significant X-ray detections from the red sequence and green valley samples, indicating the presence of a significant population of obscured AGNs among red sequence and green

valley galaxies. They concluded that their results indicate the following: (1) accretion onto the central supermassive black hole may continue after the star formation has ceased, and thus (2) if AGN feedback is responsible for the cessation of star formation in these galaxies, then the method by which this occurs does not completely remove gas from the nuclear regions.

1.2 Thesis Outline

To further our understanding of the increasingly fascinating relationship between the population of red spheroids and the supermassive black holes that inhabit them, this thesis addresses the cause and effect of significant black hole growth (a.k.a., AGNs) at $z \sim 1$. Chapter 2 begins with a description of the exquisite mulitwavelength data available for such a study (and the reasons why such data is necessary). It continues by describing the three techniques used here to select AGNs and concludes with comments regarding the amount of overlap between the various selection methods. Chapter 3 provides descriptions of the morphology measurements used to study the host galaxies of AGNs selected by the methods described in Chapter 2, and it defines various morphology classifications to be referenced in later chapters.

Employing a collection of relatively simple simulations, the next chapter probes the extent to which various methods used to measure observable characteristics (e.g., color and morphology) of AGN host galaxies are contaminated by the presence of the AGN. This is particularly relevant when determining the potential significance and

timing of any influence that an AGN might exert on the star formation rates of its host galaxy (i.e., are AGN hosts that are determined to be in the green valley actually red?) and when using the morphological characteristics of AGN hosts to study the possible relationships between interactions and the activation of the central black hole (i.e., could the many AGN host galaxies classified as bulge-dominated systems actually have disk-like or disturbed morphologies which have been hidden by light from the nuclear region?).

After quantifying the extent of the reliability of various color and morphology measurement methods, the next two chapters explain the results (based on the same color and morphology measurements) of a detailed study of the AGN host galaxies introduced in Chapter 2. Also discussed are the implications from this study regarding the causes and effects of AGNs, the relationship between AGNs and their host galaxies, the presence of the galaxy color bimodality, and the growth of the red sequence.

The final chapter begins with a summary of the conclusions described throughout this thesis, and then it goes on to provide a discussion of suggested studies which will continue to help us understand many of the facets of galaxy evolution discussed above. Throughout this thesis, $\{h, \Omega_\Lambda, \Omega_M\} = \{0.7, 0.7, 0.3\}$, and AB magnitudes are used, unless otherwise noted. In addition, numerical fractions are generally accompanied by 1-σ uncertainties, calculated following Gehrels (1986).

Chapter 2

Multiwavelength Observations, and Selection of Active Galactic Nuclei

2.1 AEGIS and GOODS-N: The Fields, the Data, and the Data Products

Determining the cause and effect of AGNs on their host galaxies, at $z \sim 1$, requires a plethora of multiwavelength data; two principal reasons are especially relevant here. For one, UV/optical/IR images and photometry are essential for determining various properties of the host galaxies, such as morphologies, stellar masses, and specific star formation rates; optical spectra are also extremely useful for the determining the redshifts. Efforts to create a complete and reliable sample of AGNs also benefit greatly from multiwavelength data. AGN selection techniques are used to identify AGNs that meet a certain set of criteria for which the technique is best suited. For example, a

sample of AGNs identified by the appearance of broad lines in their optical spectra will not include highly obscured AGNs, whereas techniques using radio power or X-ray luminosities may be better suited for the identification of such systems.

The present study makes use of the All-wavelength Extended Groth Strip International Survey (AEGIS; Davis et al. 2007) and the northern field of the Great Observatories Origins Deep Survey (GOODS-N; Giavalisco et al. 2004). The surveys provide optical images taken with the *Hubble Space Telescope*/Advanced Camera for Surveys (*HST*/ACS), optical spectra from the DEIMOS spectrograph (Faber et al. 2003) and the MMT Observatory, photometry from a variety of instruments, deep *Chandra X-ray Observatory* images, and Very Large Array (VLA) images at 1.4 GHz. The following sections describe these data in more detail.

2.1.1 AEGIS: The All-wavelength Extended Groth Strip International Survey

The Extended Groth Strip (EGS) has been studied in great detail for more than a decade (e.g., Fomalont et al. 1991; Lilly et al. 1995; Beck-Winchatz & Anderson 1999; Flores et al. 1999; Miyaji et al. 2004; Nandra et al. 2005; Georgakakis et al. 2006; Sarajedini et al. 2006). The data used here has recently been made available by the combined efforts of a large group of observers from several countries. Together, they have created the All-wavelength Extended Groth Strip International Survey (AEGIS), providing an exceptional sample of multiwavelength data well-suited for the work described here. The EGS is centered at $\alpha = 14^h17^m$, $\delta = +52°30'$, and areal coverage

Table 2.1: AEGIS observations used for the current work

Telescope/Instrument	Band, $\lambda_{\rm eff}$, or wavelength range	Limiting mag. (AB & 5σ, unless noted)	Area ($\deg^2$)
HST/ACS	V	28.14	0.197
	I	27.52	0.197
Keck/DEIMOS	6400-9100Å	$R = 24.1$	0.5
MMT Spectrograph	...	...	...
CFHT/MegaCam	u^*	26.3	1
	g'	27.0	1
	r'	26.5	1
	i'	26.0	1
	z'	25.0	1
Chandra/ACIS	2-7 keV	8.2×10^{-16} erg cm^{-2} s^{-1}	0.67
	0.5-2 keV	1.1×10^{-16} erg cm^{-2} s^{-1}	0.67
VLA	1.4 GHz/20 cm	100 μJy beam^{-1}	0.64
Spitzer/IRAC	3.6 μm	0.9 μJy	0.33
	4.5 μm	0.9 μJy	0.33
	5.8 μm	6.3 μJy	0.33
	8.0 μm	5.8 μJy	0.33
CFHT/CFH12K	B	24.5 [8σ]	1.31
	R	24.2 [8σ]	1.31
	I	23.5 [8σ]	1.31
Palomar/WIRC	J	23.0 (Vega)	0.2
	K_s	20.6 (Vega)	0.7
GALEX	NUV	25 [3σ]	1.13
	FUV	25 [3σ]	1.13

ranges from 0.0128 $\deg^2$ - 1.31 $\deg^2$, depending on the individual survey (Davis et al. 2007). Recent observations have been taken at X-ray, far-ultraviolet (FUV) and near-ultraviolet (NUV), optical (including both optical spectra and imaging), near-infrared (IR), mid-IR, and far-IR, and radio wavelengths. Please refer to Davis et al. (2007) and references therein for complete descriptions of the numerous surveys included in the AEGIS; details presented here (summarized in table 2.1.1) will focus on the data most relevant to this work.

High spatial resolution ($0.03''$/pixel) images were taken with the Advanced Camera for Surveys (ACS) on the *Hubble Space Telescope* (*HST*). These observations are available for 0.197 deg^2 of the AEGIS; the rectangular strip covers the central region of the EGS, thus overlapping with the majority of the other observations (Davis et al. 2007). The AEGIS region was observed in the F606W (V) and F814W (I) passbands to 5 σ limiting magnitudes of $V = 28.14$ and $I = 27.52$ for a point source; the limiting magnitudes are slightly lower for extended objects (Davis et al. 2007). These images have already been used by numerous authors for a variety of purposes, including a study of how galaxy mergers and morphologies evolve at $z < 1.2$ (Lotz et al. 2008a), an exploration of AGN host galaxy morphologies (Pierce et al. 2007) and a close look at the host galaxy of a dual AGN (Gerke et al. 2007), a visual search for strong gravitational lenses (Moustakas et al. 2007), and the characterization of galaxies identified as having very red IR colors (Conselice et al. 2007; Wilson et al. 2007). The *HST*/ACS-imaged galaxies in the EGS have been analyzed using codes that determine various morphology measurements, as described by Lotz et al. (2008a) and R. Griffith (in preparation); details of these measurements will be provided in the next chapter.

Optical spectra were taken with the DEIMOS spectrograph (Faber et al. 2003) on the Keck-II telescope, as part of the DEEP2 Redshift Survey (Davis et al. 2003, 2007), and with the MMT spectrograph at the MMT Observatory (A. Coil et al., in preparation). In addition to providing high quality spectroscopic redshifts, the DEEP2 optical spectra can be used to identify AGNs, as has been done recently for the AEGIS galaxies by R. Yan, following the methods described by Yan et al. (2006) and summarized below.

The DEEP2 Redshift Survey provides optical spectra for AEGIS galaxies to a limiting magnitude of $R_{AB} = 24.1$ (Davis et al. 2003, 2007). A 1200 line mm^{-1} grating was used for the survey, which covers the wavelength range of 6400-9100Å. Each target was observed for a minimum of one hour (Davis et al. 2007). After being checked by at least two observers, every redshift in the DEEP2 Redshift Survey catalog was assigned a quality code z_q indicating the level of confidence in the reliability of the redshift, where $z_q = 3$ and $z_q = 4$ indicate 95% and 99% confidence levels, respectively, in the reliabilities of the assigned redshifts. Throughout this paper, "high quality" redshifts refer to spectroscopic redshifts with $z_q \geq 3$. Within the *HST*/ACS-imaged region of the EGS, there are ∼3700 high quality DEEP2 redshifts.

The MMT spectrograph observations were designed to target AEGIS X-ray sources in an effort to improve the qualities of QSO host galaxy redshifts (A. Coil et al., in preparation). Redshifts determined from the resulting spectra were individually verified and assigned qualities having the same meanings as those that were used for the DEEP2 redshifts. Eighty-two high quality MMT redshifts are available in the EGS *HST*/ACS-imaged region, two of which are for galaxies that lack high quality DEEP2 redshifts. For the 80 galaxies that have high quality spectroscopic redshifts from *both* spectroscopic redshift surveys, the maximum difference is $\Delta_{max} = 1.43 \times 10^{-6}$, so although the MMT redshifts are used where available, it is essentially irrelevant which set of redshifts are chosen.

Supplementing the DEEP2 and MMT spectroscopic redshifts in the EGS, deep Canada-France-Hawaii Telescope Legacy Survey (CFHTLS) $u^*g'r'i'z'$ observations have

been used by multiple authors to determine photometric redshifts of four fields (e.g., Lilly et al. 1995; Ilbert et al. 2003; S. Gwyn et al., in preparation; J.-S. Huang, in preparation). The 1 $\deg^2$ CFHTLS field D3 includes the EGS but does not completely encompass the *HST*/ACS-imaged region. The observations used for AEGIS studies have exposure times (in hours) and limiting magnitudes of 1.7/26.3, 1.8/27.0, 4.1/26.5, 13.0/26.0, and 1.0/25.0 in the u^*, g', r', i', and z' passbands, respectively

Huang provides ∼6900 photometric redshifts in the *HST*/ACS-imaged region of the EGS; ∼3900 of these match galaxies for which we do not have high quality spectroscopic redshifts. For the 3055 galaxies that have both photometric redshifts and high quality spectroscopic redshifts, the spectroscopic redshifts are always preferred. Following Ilbert et al. (2006), a catastrophic error in the determination of the photometric redshift is defined to have occured when $|\Delta z|/(1+z) > 0.15$. Based on the 3055 galaxies for which photometric and spectroscopic redshifts are available, it is determined that 2.26% of the photometric redshifts suffer catastrophic failures; this fraction decreases to 2.18% if the photometric redshifts are constrained to the range $0.2 < z < 1.2$.

Figure 2.1 shows the spectroscopic and photometric redshift for galaxies at $z < 2$. As indicated on the figure, the upper panels feature AEGIS galaxies, and the left and right panels of each row show the spectroscopic and photometric redshift distributions, respectively. For the sake of clarity, the peak of each distribution is scaled to 100, thus the vertical scale is arbitrary.

The *Chandra X-ray Observatory* Advanced CCD Imaging Spectrograph (ACIS) instrument observed a strip of eight pointings (0.67 $\deg^2$ total area) in the EGS for

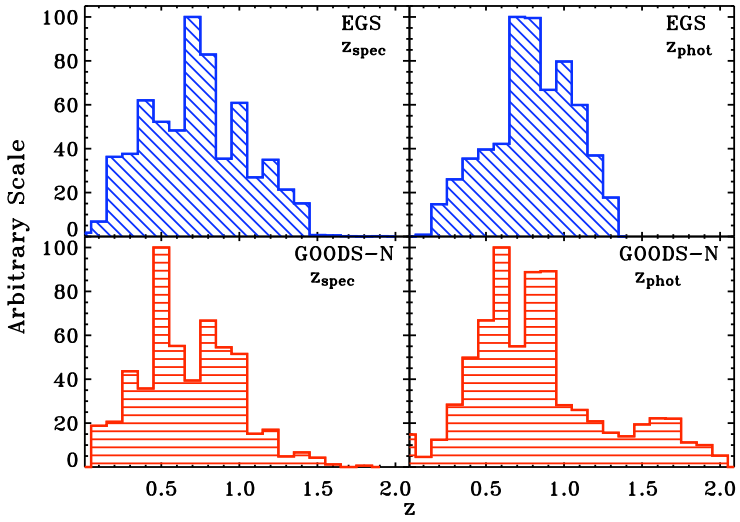

Figure 2.1: Spectroscopic and photometric redshifts of AEGIS and GOODS-N galaxies in the *HST*/ACS-imaged regions.

approximately 200 ks per pointing (Nandra et al. 2005; Davis et al. 2007; Laird et al. 2008), and additional observations of three of the central pointings are underway. Once complete, these three pointings will have been imaged for a total of 800 ks each. Laird et al. (2008) presented the AEGIS-X survey (comprised of the 1325 X-ray sources detected in the EGS) and the methods used to reduce and analyze the observations. As they described, X-ray "sources" are defined as X-ray-detected objects that have Poisson detection probability thresholds $< 4 \times 10^{-6}$; in other words, 5-σ detections are required.

At $z = 1$, the on-axis flux limit for hard-band[1]-selected sources (3.76×10^{-16} erg cm^{-2} s^{-1}) corresponds to $L_{2-10\ \mathrm{keV}} = 2.4 \times 10^{42}$ erg s^{-1}. This slightly exceeds the minimum luminosity used to define the sample of X-ray-selected AGNs described below, which means that although the X-ray AGN sample is complete at low redshifts,

[1]X-ray energy bands: full (0.5-7 keV), soft (0.5-2 keV), hard (2-7 keV), and ultra-hard (4-7 keV)

it may miss some of the lower luminosity AGNs at the higher redshifts. Georgakakis et al. (2008) described the methods used to match X-ray sources to galaxies in included as part of the DEEP2 Redshift Survey, and the current work uses the resulting matched catalogs. Using an early version of the *Chandra* observations, Nandra et al. (2007) examined the color-magnitude relationship of X-ray-selected AGNs, and Fang et al. (2007) presented the X-ray characteristics of groups and clusters found by the DEEP2 Redshift Survey. The final 200-ks X-ray observations were used by Bundy et al. (2008) to study the possible link between AGNs and the quenching of star formation.

VLA observations at 1.4 GHz were used to create samples of high-power radio sources and radio-selected AGNs. The AEGIS data were taken in the VLA's B configuration for 18 hours per pointing (Davis et al. 2007; Ivison et al. 2007). The B configuration provides an antenna distribution with maximum spacing of 11.4 km and a circular synthesized beam of width $3.8''$ at 1.4 GHz; the corresponding PSF is $4.2''$ (Davis et al. 2007). For this survey, which covered an area of 0.64 deg^2, the noise level was 10μJy beam^{-1}, with a limiting flux density of $S_{1.4/\mathrm{GHz}} = 50\mu$Jy, which corresponds to a rest-frame 1.4 GHz power $P_{1.4\ \mathrm{GHz}} = 2.3 \times 10^{23}$ W Hz^{-1} at $z = 1$ (Ivison et al. 2007). Unlike the AEGIS X-ray AGN sample, the AEGIS radio AGN sample (defined below) is complete out to high redshifts because the radio power criteria used to define the AGN sample significantly exceeds the power corresponding to the limiting flux density. Ivison et al. (2007) stacked radio sources from the AEGIS20 catalog that they presented to explore the characteristics of several galaxy populations, and Le Floc'h et al. (2007) examined the radio emissions from an ultraluminous starburst. Willner et al.

(2006) presented observations of the EGS taken at 4.8 GHz; these are not used here.

The *Spitzer Space Telescope*/Infrared Array Camera (IRAC) observations of the EGS at 3.6/4.5/5.8/8.0 μm cover an area 0.33 deg^2, approximately enclosing the *HST*/ACS-imaged region, to limiting magnitudes of 0.9/0.9/6.3/5.8 μJy; the PSF for each of the bands is $\sim 2''$ (Davis et al. 2007). A full catalog was presented by Barmby et al. (2008), and it has been used, in combination with the AEGIS20 radio catalog, by Park et al. (2008) to identify and study a sample of obscured AGNs. In addition, S. P. Willner et al. have matched the IRAC observations to radio sources, minimizing the problem related to matching radio sources (with the large PSF) to *HST*/ACS images; the results from Willner et al. are used here. The EGS has also been observed by the *Spitzer*/Multiband Imaging Photometer for *Spitzer* (MIPS; Davis et al. 2007). Although the MIPS observations are not used for the current work, they have been combined with IRAC and *Chandra* observations by Alonso-Herrero et al. (2004) and Barmby et al. (2006) to study systems detected at both the X-ray and IR wavelengths.

Bundy et al. (2006) described the measurement of galaxy stellar masses in the four DEEP2 fields, based on BRI observations taken with the CFHT/CFH12K mosaic camera (Cuillandre et al. 2001) and K_s band images from the Wide-Field Infrared Camera (WIRC) on the Palomar 5-m telescope. The BRI observations cover a 1.31 deg^2 region of the EGS to limiting magnitudes of 24.5, 24.2, and 23.5, respectively, and the Palomar/WIRC K_s imaging of the EGS is complete to $K_s = 20.6$ (Vega; Davis et al. 2007); both sets of observations completely overlap the *HST*/ACS-imaged region. (The J band images taken with the Palomar/WIRC are not used for the current work.)

For the DEEP2 fields, Bundy et al. (2006) first created a spectral energy distribution (SED) for each galaxy based on the $BRIK_s$ observations. The observed SEDs were then compared to a grid of synthetic SEDs (Bruzual & Charlot 2003) exhibiting a range of properties, including star-formation histories, ages, metallicities, and dust content. At each point on the grid Bundy et al. calculated the stellar mass, minimum χ^2, and the probability that the synthetic SED represented the observed SED, assuming an initial mass function (IMF) from Chabrier (2003). Each galaxy was then assigned the median stellar mass of the corresponding probability distribution. The work by Bundy et al. provides us with stellar masses for 3382 AEGIS galaxies in the *HST*/ACS-imaged region.

A *Galaxy Evolution Explorer* (*GALEX*; Martin et al. 2005; Morrissey et al. 2005, 2007) observation of the EGS covers a 1.13 deg^2 circular region of the EGS, completely encompassing the region observed by the *HST*/ACS, to a 3-σ limiting magnitude of 25 in both the NUV and FUV (Davis et al. 2007). Ivison et al. (2007) used these data, as well as other AEGIS data, to explore the radio characteristics of a sample of UV-selected galaxies.

Applying the methods described by Salim et al. (2005, 2007) to AEGIS galaxies, S. Salim combined *GALEX* and CFHTLS $u^*g'r'i'z'$ observations with K_s-band photometry to calculate rest-frame UV-optical colors ($NUV - R$). For nearby Type-2 (narrow-line) AGNs, Kauffmann et al. (2007) showed that UV-optical colors are reliable tracers of the star formation occuring in the outer parts of a galaxy, and the colors are not biased by the presence of an AGN. However, UV emissions from Type-1 (broad-line)

AGNs may heavily contaminate the measured galaxy colors, so galaxies whose DEEP2 spectra fit a template for Type-1 AGNs were excluded from the determination of the UV-optical colors.

Specific star formation rates (SSFR=SFR/M_*) were then derived from the UV-optical colors, using a Chabrier (2003) IMF. Use of the UV continuum to constrain SFRs was supported by Kennicutt (1998) because of the strong connection between the UV continuum and emissions from young stellar populations, but he also cautioned that this method is particularly sensitive to extinction and the selected IMF. The choice of the Chabrier (2003) IMF offers a measure of consistency between the SSFRs derived by S. Salim and the stellar masses measured by Bundy et al. (2006). Throughout the analyses described here, references to blue, green, and red *UV-optical* colors indicate $NUV - R < 3$, $3 < NUV - R < 4.5$, and $NUV - R > 4.5$, respectively.

Using observed colors from the CFHT/CFH12K BRI observations, DEEP2 redshifts, and a set of galaxy spectral energy distributions (SEDs) from Kinney et al. (1996), Willmer et al. (2006) estimated the appropriate K-corrections and rest-frame $U - B$ colors for nearly all of the galaxies then available in the four DEEP2 Redshift Survey fields. Although this initially included only a small fraction of the AEGIS galaxies, the rest-frame optical colors and magnitudes of almost 99% of the galaxies in the *HST*/ACS-imaged region have now been determined. Willmer et al. found that the root-mean-square (rms) errors for the rest-frame colors and the K-correction between R and B (K_{RB}) depended strongly on redshift. Galaxies with redshifts allowing significant overlap between the observed bands and the Kinney et al. SEDs experienced the smallest

errors ($U-B$: 0.03 mag; K_{RB}: 0.01 mag), while at $z \geq 1.2$ the measurements attained larger errors ($U-B$: 0.12 mag; K_{RB}: 0.15 mag; Willmer et al. 2006). Following Willmer et al. (2006) and Nandra et al. (2007), the current work uses the following optical colors:

$$\text{Red}: \ U - B > -0.032(M_B + 21.52) + 0.454 - 0.25 + 0.05 \ \text{ and} \tag{2.1}$$

$$\text{Blue}: \ U - B < -0.032(M_B + 21.52) + 0.454 - 0.25 - 0.05; \tag{2.2}$$

green optical colors are those $U-B$ values that fall between the red and blue colors.

2.1.2 GOODS-N: The Northern Field of the Great Observatories Origins Deep Survey

Giavalisco et al. (2004) described the optical and near-IR observations taken of the northern and southern fields of the Great Observatories Origins Deep Survey (GOODS). Research presented in the current work is based in part on observations taken of the northern field (GOODS-N), portions of which are also known as the Hubble Deep Field-North (HDF-N; Williams et al. 1996; Ferguson et al. 2000) and the *Chandra* Deep Field-North (CDF-N; Brandt et al. 2001; Alexander et al. 2003) because of early observations taken with the specified instruments. The GOODS-N field is centered at $\alpha = 12^{\rm h}36^{\rm m}55^{\rm s}$, $\delta = 62^{\circ}14^{\rm m}15^{\rm s}$ (J2000.0; Giavalisco et al. 2004). Prior to and in the few intervening years since publication of the report by Giavalisco et al., many others have presented detailed accounts of additional observations of the GOODS-N field, taken with a multitude of instruments (e.g., Brandt et al. 2001; Alexander et al. 2003; Capak et al. 2004; Wirth et al. 2004; Biggs & Ivison 2006), and numerous scientific results

Table 2.2: GOODS-N observations used for the current work

Telescope/Instrument	Band, $\lambda_{\rm eff}$, or wavelength range	Limiting mag. (AB & 5σ, unless noted)	Area ($\deg^2$)
HST/ACS	B	<27.8 [10σ]	0.044
	V	<27.8 [10σ]	0.044
	i	<27.1 [10σ]	0.044
	z	<26.6 [10σ]	0.044
Keck/DEIMOS	4800-9800Å	$R = 24.4$	...
KPNO/MOSAIC	U	27.1	0.40
Subaru/SuprimeCam	B	26.9	0.27
	V	26.8	0.27
	R	26.6	0.27
	I	25.6	0.27
	z'	25.4	0.27
UH/QUIRC	HK'	22.1	0.11
Chandra/ACIS	2-8 keV	1.4×10^{-16} erg cm^{-2} s^{-1}	0.029
	0.5-2 keV	2.5×10^{-17} erg cm^{-2} s^{-1}	0.029
VLA	1.4 GHz/20 cm	20 μJy beam^{-1}	0.089
Palomar/WIRC	K_s	22.4	< 0.062

coming from these observations (e.g., Alexander et al. 2002; Barger et al. 2003, 2005, 2007; Bundy et al. 2005; Donley et al. 2005; Grogin et al. 2005; Laird et al. 2005). Details relevant to the current work are presented in Table 2.1.2.

HST/ACS observations provide high spatial resolution ($0.03''$/pixel) images for 0.044 deg^2 of the GOODS-N (Giavalisco et al. 2004). The GOODS-N region was observed in the F435W, F606W, F775W, and F850LP passbands ($BViz$) to 10σ limiting magnitudes of better than 27.8 (BV), 27.1 (i), and 26.6 (z; Giavalisco et al. 2004). Grogin et al. (2005) used these images to characterize the morphologies of a sample of X-ray-selected AGNs from this field, and stellar masses determined by Bundy et al. (2005) were based in part on photometry derived from the *HST*/ACS images. GOODS-N *HST*/ACS-imaged galaxies have also been analyzed using the code described by Lotz

et al. (2008a) to determine various morphology measurements; details of these measurements will be provided in the next chapter.

Optical spectra in the GOODS-N are provided by the Team Keck Redshift Survey (TKRS) for galaxies to a limiting magnitude of $R_{AB} = 24.4$ (Wirth et al. 2004). This survey used the 600 lines mm^{-1} grating on the DEIMOS instrument (Faber et al. 2003) and has a wavelength coverage of 4600-9800Å. As for the DEEP2 Redshift Survey (Davis et al. 2003, 2007), every target was observed for an hour. High quality TKRS redshifts are defined as those with qualities $Q = 3$ (90% confidence) or $Q = 4$ (99% confidence). The *HST*/ACS-imaged region of the GOODS-N contains 844 galaxies that have high quality ($Q = 3, 4$) TKRS redshifts. These spectra can also be used to identify active galaxies, following the methods described by Yan et al. (2006), and fifty-three additional spectroscopic redshifts were determined by R. Yan while doing so.

The central 0.2 deg^2 of the GOODS-N was observed in the $UBVRIz'HK'$ bands to 5-σ limiting magnitudes of 27.1, 26.9, 26.8, 26.6, 25.6, 25.4, 22.8, and 22.8, respectively (Capak et al. 2004). The region was observed using the MOSAIC prime focus camera on the Mayall 4-m telescope at the Kitt Peak National Observatory (U; Jacoby et al. 1998; Muller et al. 1998; Wolfe et al. 1998), the Suprime-Cam instrument on the Subaru 8.2-m telescope ($BVRIz'$; Miyazaki et al. 2002), and the QUIRC camera on the 2.2-m telescope at the University of Hawaii (HK'; Hodapp et al. 1996).

Wirth et al. (2004) briefly explained the derivation of photometric redshifts for the GOODS-N, using the $UBVRIz'HK'$ observations described by Capak et al. (2004) to estimate redshifts, and a Bayesian code (Benitez 2000) to assess the reliability

of the redshift estimates. Upon comparing the photometric redshifts to the TKRS spectroscopic redshifts, they found that only 3% of the photometric redshifts differ by more than 30% from the spectroscopic redshifts (Wirth et al. 2004). In the *HST*/ACS-imaged region of the GOODS-N, there ∼4800 photometric redshifts, of which ∼3900 correspond to GOODS-N galaxies lacking high quality spectroscopic redshifts. Following Ilbert et al. (2006), a catastrophic error in the determination of the photometric redshift has occured when $|\Delta z|/(1+z) > 0.15$. Based on the 897 galaxies for which photometric and spectroscopic redshifts are available, it is determined that 7.13% of the photometric redshifts suffer catastrophic failures; this fraction increases to 7.95% if the photometric redshifts are constrained to the range $0.2 < z < 1.2$. Wirth et al. (2004) also explained that this set of observations has been used to calculate rest-frame optical $(U-B)$ colors of many of the GOODS-N galaxies, by combining Kinney et al. (1996) SEDs with the *HST*/ACS CCD and filter throughputs.

Figure 2.1 shows the spectroscopic and photometric redshift distributions for galaxies at $z < 2$. As indicated on the figure, the lower panels feature GOODS-N galaxies. The left and right panels of each row show the spectroscopic and photometric redshift distributions, respectively. For the sake of clarity, the peak of each distribution is scaled to 100, so the vertical scale is arbitrary.

At almost 2 Ms, the GOODS-N *Chandra* images are the deepest X-ray observations currently available (e.g., Alexander et al. 2003), and even though some shallower X-ray surveys (e.g., XBootes: Murray et al. 2005; AEGIS-X: Laird et al. 2008) surpass the area of the GOODS-N *Chandra* image (∼0.12 deg^2), this single pointing allows the

study of more than 500 X-ray sources. Many authors have already taken advantage of this deep X-ray data, studying, for example, X-ray properties of different galaxy populations (Brandt et al. 2001; Alexander et al. 2002), host galaxy morphologies of X-ray-selected AGNs (Grogin et al. 2005), and the evolution of X-ray-selected AGNs (Barger et al. 2005).

Laird et al. (2005) analyzed the central 0.029 deg^2 of the *Chandra* image, and the results of their analysis is used for the current work. As mentioned previously, X-ray sources are defined as those objects with Poisson detection probability thresholds $< 4 \times 10^{-6}$, a 5-σ detection. At $z = 1$, the on-axis flux limit for hard-band-selected sources in the GOODS-N corresponds to $L_{2-10\ \mathrm{keV}} = 7.6 \times 10^{41}$ erg s^{-1}. The longer GOODS-N observation leads to the identification of several X-ray sources below the detection limits of the EGS survey at most redshifts, but fewer than 20 of these correspond to X-ray sources classified as AGNs.

A region of the GOODS-N covering approximately 0.089 deg^2 has been observed by the VLA at 1.4 GHz for a total of 50 hours (Richards 2000). The observations were taken with the VLA in the A configuration, providing an antenna distribution with a maximum spacing of 36.4 km and a synthesized beamwidth of 1.52″. Biggs & Ivison (2006), whose results are used here, reduced 45 hours of the GOODS-N VLA observations, choosing to exclude the initial several hours, which had been taken several weeks earlier and using a slightly different observing strategy than the majority of the observations. They identified 537 radio sources and reported a noise level of 5.8μJy beam^{-1}, with a 5-σ flux limit of 20μJy beam^{-1} (Biggs & Ivison 2006). At $z = 1$, this

flux limit corresponds to a rest-frame 1.4-GHz power $P_{1.4\ \mathrm{GHz}} = 9.1 \times 10^{22}$ W Hz^{-1}, indicating that the sample of radio-selected AGNs in the GOODS-N (defined below) will be complete.

Stellar masses of GOODS-N galaxies were determined by Bundy et al. (2005), following the general methods described above for AEGIS galaxies. *HST*/ACS observations (Giavalisco et al. 2004) provided the necessary $BVIz'$ photometry, and Bundy et al. used the WIRC on the Palomar Observatory Hale 5-m telescope to collect K_s-band imaging. Three observations were carried out, covering ∼70% of the GOODS-N, and the final K-band catalog used by Bundy et al. had a limiting magnitude of $K_s = 22.4$. Bundy et al. (2005) provided stellar masses for 947 galaxies in the *HST*/ACS region of the GOODS-N.

2.2 Selection of Active Galactic Nuclei

Active nuclei can be identified using a variety of techniques, each based on a subset of the characteristics unique to AGNs, including extreme luminosities and unique signatures in their optical spectra. Although our inability to directly observe activity in the immediate vicinity of a black hole (i.e., at radii $< 10^{17}$cm) makes it impossible to fully explain the origins of the observed activity, observations continue to provide important clues to the inner workings of these systems. It seems clear that massive galaxies contain correspondingly massive black holes in their nuclear regions ($M_{\mathrm{BH}} \sim 10^{-4} \times M_{\mathrm{sph}}$; e.g., Ferrarese & Merritt 2000; Gebhardt et al. 2000), and the

activity associated with AGNs is believed to be related to the growth of these black holes as they feed on nuclear gas (e.g., Peterson 1997). The relativistic speeds reached by infalling gas particles (which probably form an accretion disk around the black hole) cause the emission of synchrotron radiation, which is then observed as an approximate power-law continuum at high frequencies; the power-law turns over as the gas becomes optically thick at lower (e.g., radio) frequencies (Peterson 1997).

Just beyond the accretion disk is a region believed to be responsible for the broad emission lines associated with Type-1 Seyfert galaxies; however, this broad-line region (BLR) is still too close to the black hole to be well-studied. Spatial resolution begins to be achieved for the narrow-line region (NLR), which is identifiable for both Type-1 and Type-2 Seyfert galaxies. Careful studies have revealed an approximate continuum, with respect to the strength of observable broad lines, between the two types of Seyfert galaxies (e.g., Osterbrock 1981). In addition, AGNs are commonly identified by X-ray, radio, and infrared characteristics that are clearly due to causes other than star formation. For example, Condon (1992) reported that the 1.49-GHz radio power associated with normal galaxies (i.e., non-active with respect to significant black hole growth) is not likely to exceed $L_{1.49\ \mathrm{GHz}} \sim 2 \times 10^{23}$ W Hz^{-1}; radio powers exceeding this by an order of magnitude or more indicate significant nuclear activity.

Attempts to explain some of the observed differences (e.g., the presence or absence of the BLR) between samples of AGNs identified using various techniques has led to unification schemes. Typically, the basic idea is that the observed characteristics of many types of AGNs depend strongly on the line-of-sight between an observer and the

nuclear source of the continuum emission. A likely explanation involves the presence of a dusty torus surrounding the nuclear region and obscuring the BLR in certain directions. Thus, an observer may catch a glimpse of the BLR if the torus is oriented such that the observer's line-of-sight coincides with the unobscured cone-shaped region on either side of the torus, but would be limited to studying the NLR if the line-of-sight runs into the torus (e.g., Osterbrock 1978). Partial observations of the BLR may be explained by the presence of a scattering medium in the unobscured cone, such as free electrons, which could reveal the BLR in polarized light (e.g., Antonucci & Miller 1985; Tran et al. 1992).

For the current work, AGNs are selected based upon hard (2-10 keV) X-ray luminosity, 1.4-GHz radio power, and/or AGN signatures in the optical spectra. Each of these techniques, described in detail below, identifies AGNs that are not necessarily selected by either of the other techniques, thereby increasing the completeness of the AGN sample as a whole, while also allowing the study of the occasionally unique characteristics associated with the AGNs (and their host galaxies) identified by a given method.

2.2.1 X-ray Selection

AEGIS X-ray sources were matched to DEEP2 galaxies using the Likelihood Ratio method (e.g., Ciliegi et al. 2003; Georgakakis et al. 2008). GOODS-N X-ray sources were matched to optical counterparts by requiring that the positional offset between the X-ray source and a potential host galaxy not exceed $1.5''$ for *Chandra*

off-axis angles (OAAs) $< 5.0'$ or $2.0''$ for OAAs $\geq 5.0'$. The average offsets were then added to the optical positions, and the sources were rematched, using the same maximum positional offset criteria. If a GOODS-N X-ray source was within the allowed distance of multiple optically detected galaxies, the nearest object was selected as the host galaxy. Four of the X-ray sources had two potential hosts during the final matching, and in each case, the difference between the two positional offsets exceeded $0.5''$, so that the closer of the two potential host galaxies was clearly a better match to the X-ray source; none of the X-ray sources were matched to more than two potential host galaxies.

After matching the X-ray sources to optical counterparts (and thus redshifts), the method described by Teng et al. (2005) was used to convert the X-ray flux in each of the four energy bands to a 2-10 keV flux, using an assumed power-law slope $\Gamma = 1.4$ (e.g., Peterson 1997). Hard X-ray luminosities $L_{2-10\ \mathrm{keV}}$ were then calculated using the extrapolated 2-10 keV fluxes and the best available redshifts. In order of decreasing preference, the final X-ray luminosity assigned to an X-ray source was based on the flux from the full, soft, hard, or ultra-hard band (i.e., if the X-ray source did not have a significant detection in the full-band, then the assigned luminosity was based on the soft band, the hard band, or the ultra-hard band). The order of preference corresponds to the sensitivity of the bands; the more sensitive bands received higher preference. Combining the GOODS-N and AEGIS samples, 276 X-ray luminosities were derived from full-band fluxes, 22 were derived from soft-band fluxes, two were derived from hard-band fluxes, and one was derived from the ultra-hard-band flux.

Significant hard-band X-ray luminosities are often used to identify AGNs, be-

cause only the less energetic (i.e., 0.5-2 keV) and/or less luminous X-ray emissions are expected to orginate in star formation processes (e.g., Grogin et al. 2003, 2005; Barger et al. 2005; Laird et al. 2005). The current work implements $L_{2-10\ \mathrm{keV}} > 10^{42}$ erg s^{-1} as the criterion for X-ray-selected AGNs (e.g., Grogin et al. 2005; Barger et al. 2007), an order of magnitude higher than a conservative cut observed by Laird et al. (2005), who sought to exclude AGNs from their sample. Thus, the X-ray-selected AGN sample used here should be fairly pure, though it may exclude a few low-luminosity AGNs.

Figure 2.2 shows the 2-10 keV luminosity as a function of redshift for AEGIS (red symbols) and GOODS-N (blue symbols) X-ray sources with redshifts $z < 2$. Open squares represent X-ray sources that are also radio sources, 'S's represent X-ray sources that are selected as AGNs based on their optical spectra, filled diamonds represent X-ray sources that are both radio sources *and* optical spectra-selected AGNs, and 'x's represent X-ray sources that are *neither* radio sources *nor* optical spectra-selected AGNs.

The black vertical and horizontal lines at $L_{2-10\ \mathrm{keV}} = 10^{42}$ erg s^{-1}, $z = 0.2$, and $z = 1.2$, enclose the sample of X-ray-selected AGNs discussed in the current work. Also plotted are the on-axis flux limits, as a function of redshift, for the AEGIS (blue dashed curve) and the GOODS-N (red dash-triple dotted curve). As expected, at high redshifts the deeper GOODS-N observation detects several AGNs at X-ray luminosities below the AEGIS flux limits. At redshifts $0.2 < z < 1.2$, 95 X-ray-selected AGNs were identified in the AEGIS and 91 were identified in the GOODS-N.

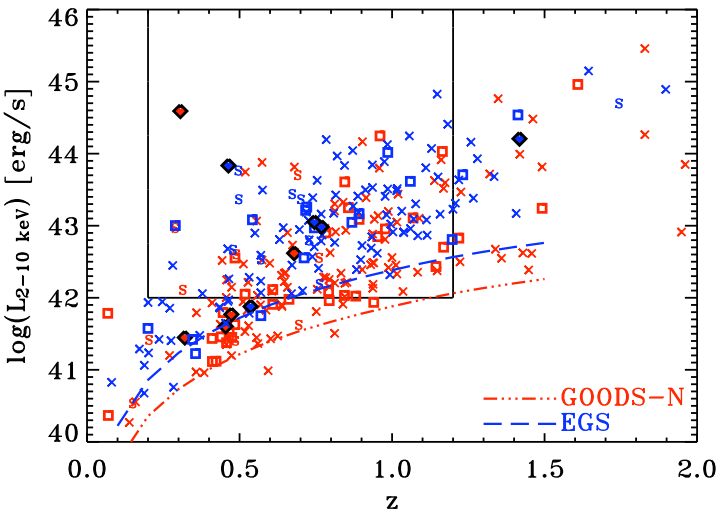

Figure 2.2: X-ray luminosity vs. redshift for AEGIS and GOODS-N X-ray sources.

2.2.2 Radio Selection

AEGIS radio sources (5-σ detections) were initially matched to *Spitzer*/IRAC images by S. P. Willner et al., who identified matches for both compact and extended radio sources. Radio source positions derived from the *Spitzer*/IRAC images were then matched to galaxy positions derived from *HST*/ACS images; successful matches were indicated by positional offsets of less than 0.5″. The average offsets from the successful matches were added to the *HST*/ACS-derived positions, and the sources were re-matched, again allowing a maximum offset of 0.5″. The AEGIS radio survey does not include the southern-most end of the *HST*/ACS observations, thereby excluding any radio sources in this region. Based on the small size of the AEGIS radio sample, it is estimated that no more than a dozen radio sources would be excluded, up to ∼4 of

which might have high radio powers.

GOODS-N radio sources were matched directly to the optical images, using a method similar to the matching between GOODS-N X-ray sources and their optical counterparts, except that the maximum offset was not varied with the distance from the center of the VLA observation. There were no cases where a radio source was matched to multiple optical sources within the maximum positional offset. The GOODS-N radio survey completely encloses the *HST*/ACS region, excluding the potential for missing sources.

After radio sources were matched to the *HST*/ACS counterparts, 1.4-GHz radio powers $P_{1.4\ \mathrm{GHz}}$ (W Hz^{-1}) were calculated based on the measured radio fluxes and the best available redshift for each galaxy, assuming a radio spectral index $\alpha = 0.8$, where $S_\nu \propto \nu^{-\alpha}$ (e.g., Condon 1992). [Note that some authors define $S_\nu \propto \nu^{+\alpha}$ (e.g., Thompson et al. 2006; Seymour et al. 2008); their radio spectral indices have the opposite sign with respect to the convention used here.] A radio spectral index $\alpha = 0.8$ corresponds to synchrotron emission from star formation (e.g., Condon 1992; Seymour et al. 2008), thus the derived radio powers indicate the star-formation rates (SFRs) implied by the observed radio fluxes. The criterion implemented here for radio power-based AGN selection, $P_{1.4\ \mathrm{GHz}} > 10^{25}$ W Hz^{-1}, represents an unrealistically high SFR, as suggested by Condon (1992) and the exercise explained below.

Approximately 44% of the AEGIS galaxies at $0.2 < z < 1.2$ have stellar masses from Bundy et al. (2006), nearly 90% of which are $< 10^{11} M_\odot$. Figure 1 of Noeske et al. (2007) indicates that a $10^{11} M_\odot$-galaxy at $z \approx 1$ has a SFR of 40 $M_\odot$

yr^{-1}. Combining equations (21) and (23) from Condon (1992), which relate the SFR to the radio power originating from star formation and from HII regions, and using the conditions specified by Haarsma et al. (2000), we find that a SFR of 40 $M_{\odot}$ yr^{-1} corresponds to $P_{1.4\ \mathrm{GHz}} \sim 3 \times 10^{22}$ W Hz^{-1}, which is 2-3 orders of magnitude below our radio power criterion. Approaching it from the other direction, a radio power $P_{1.4\ \mathrm{GHz}} = 10^{25}$ W Hz^{-1} corresponds to a SFR$\approx$12,000 $M_{\odot}$ yr^{-1}, which is well above the relation indicated by Figure 1 of Noeske et al. (2007).

Attenuation of radio emissions due to ionized gas surrounding the nuclear regions of a galaxy may result in observed radio fluxes that represent lower limits to the intrinsic radio fluxes, suggesting that some of the radio sources with 1.4-GHz powers slightly lower than the criterion may also be AGNs. Therefore, while maintaining the high-power criterion for "AGNs", the characteristics of lower power radio sources (10^{24} W $Hz^{-1} < P_{1.4\ \mathrm{GHz}} < 10^{25}$ W Hz^{-1}) are also studied. Figure 2.3 shows the 1.4 GHz power as a function of redshift for AEGIS (blue symbols) and GOODS-N (red symobls) radio sources. 'x's represent radio sources that are also X-ray sources, 'S's represent radio sources that are selected as AGNs based on their optical spectra, filled diamonds represent radio sources that are both X-ray sources *and* optical spectra-selected AGNs, and open squares represent radio sources that are *neither* X-ray sources *nor* optical spectra-selected AGNs.

The solid black vertical and horizontal lines at $P_{1.4\ \mathrm{GHz}} = 10^{25}$ W Hz^{-1}, $z = 0.2$, and $z = 1.2$ enclose the sample of radio-selected AGNs discussed in the current work. The dotted horizontal line at $P_{1.4\ \mathrm{GHz}} = 10^{24}$ W Hz^{-1} represents the lower boundary of

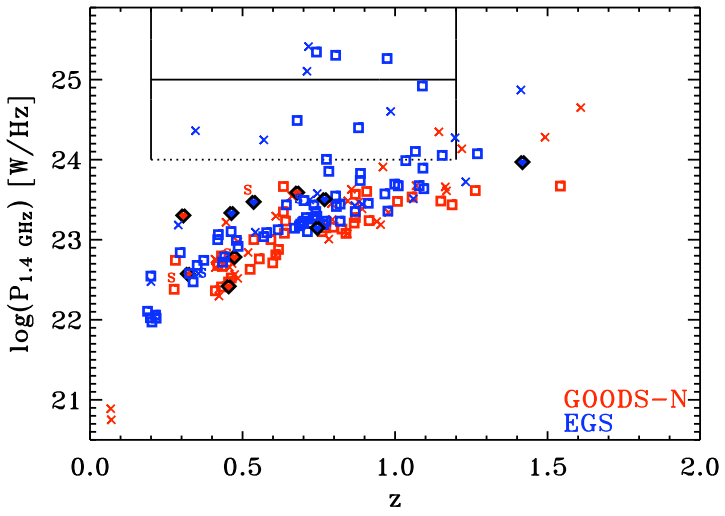

Figure 2.3: Radio power vs. redshift for AEGIS and GOODS-N radio sources.

the "high-power" radio source criterion. At redshifts $z < 1$, this lower boundary seems to separate the radio sources into two distinct populations, supporting the decision to study all of the sources that have $P_{1.4\ \mathrm{GHz}} > 10^{24}$ W Hz^{-1}. At redshifts $0.2 < z < 1.2$, 15 high-power radio sources were identified from the AEGIS and one was identified in the GOODS-N.

2.2.3 Optical Spectroscopy Selection

The optical spectra-selected AGNs discussed here are a combination of Type-2 Seyfert galaxies, broad-line AGNs (BLAGNs), LINERs, and systems that are clearly active, but whose AGN class is difficult to specify using currently available spectral data; such objects are classified as "ambiguous". Most of the optical spectra-selected

AGNs, identified by R. Yan (following Yan et al. 2006), were identified based on spectral emission-line equivalent widths and flux ratios, along with $U - B$ galaxy colors.

Selection of the LINER sample required DEIMOS spectrograph observations of [OII] and Hβ, a 2σ detection of the [OII] line, red $U - B$ galaxy colors (as defined by Willmer et al. 2006), and an [OII] equivalent width exceeding $18\times$H$\beta - 6$ (Yan et al. 2006). Spectral coverage for the Seyfert galaxy sample needed to include [OIII] and Hβ, with a 2σ detection required for the [OIII] line; the galaxy colors were required to exceed $U - B = 0.8$. If the Hβ detection significance was at least 2σ, then the final criterion for the Seyfert galaxy sample was an emission-line flux ratio [OIII]/H$\beta > 3$; otherwise, this inequality represented a required lower limit. In the AEGIS, two broad-line AGNs were identified, and the optical colors assigned to their host galaxies were significantly bluer ($U - B < 0.5$) than the host galaxy colors of the majority of the optical spectra-selected AGNs.

Due to the differing AEGIS and GOODS-N spectral wavelength coverage, LINERs could be identifed at $0.7 < z < 0.8$ (AEGIS) and $0.2 < z < 1.0$ (GOODS-N), while Seyferts could be identified at $0.3 < z < 0.8$ (AEGIS) and $z < 1.0$ (GOODS-N). The following analyses combined LINERs, Seyferts, BLAGNs, and ambiguous AGNs from the AEGIS and GOODS-N; thus, the final redshift range of the sample of optical spectra-selected AGNs was approximately $0.2 < z < 0.9$. The $U - B$ colors of the galaxies hosting these AGNs were also significantly restricted by the selection criteria, and these restrictions are clearly shown by Figure 2.4, a plot of the $U - B$ colors and redshifts of the host galaxies of optical spectra-selected AGNs from the AEGIS (blue symbols)

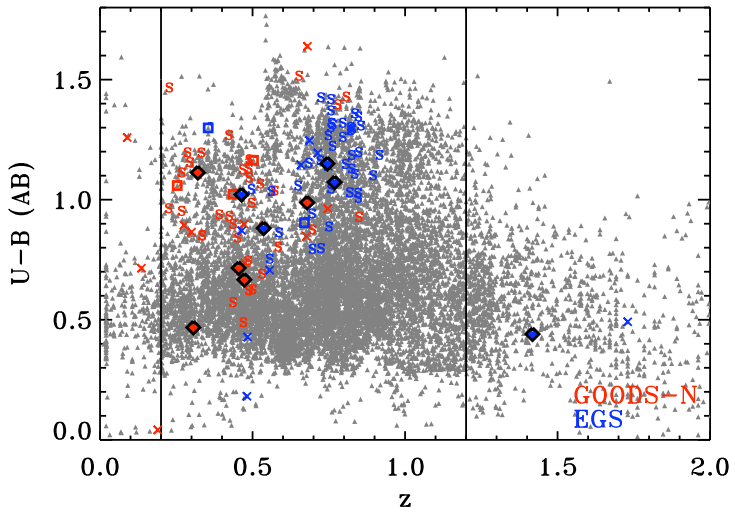

Figure 2.4: $U - B$ color vs. redshift for host galaxies of AEGIS and GOODS-N optical spectra-selected AGNs.

and the GOODS-N (red symbols). 'x's represent optical spectra-selected AGNs that are also 5-σ X-ray sources, open squares represent AGNs that are also 5-σ radio sources, filled diamonds represent AGNs that are both X-ray sources *and* radio sources, and 'S's represent optical spectra-selected AGNs that are *neither* X-ray sources *nor* radio sources. The small gray symbols represent *all* the galaxies in the AEGIS and GOODS-N for which reliable redshifts and optical colors are available.

The vertical lines at $z = 0.2$ and $z = 1.2$ enclose the sample of optical spectra-selected AGNs discussed in the current work. The 52 optical spectra-selected AGNs in the AEGIS sample are divided almost equally between LINERs and narrow-line Seyfert galaxies, in addition to two BLAGNs (both of which are X-ray-selected AGNs, but because of the incomplete overlap between the X-ray and radio surveys, the radio

Table 2.3: Summary of X-ray-selected AGNs, high-power radio sources, and optical spectra-selected AGNs, at $0.2 < z < 1.2$.

Sample	# of Objects (Total / AEGIS / GOODS-N)
All	281 / 147 / 134
$L_{2-10\ \mathrm{keV}} > 10^{42}$ erg s^{-1}	186 / 95 / 91
$P_{1.4\ \mathrm{GHz}} > 10^{24}$ W Hz^{-1}	16 / 15 / 1
Optical spectra-selected AGNs	102 / 52 / 50
$L_{2-10\ \mathrm{keV}} > 10^{42}$ erg s^{-1} & $P_{1.4\ \mathrm{GHz}} > 10^{24}$ W Hz^{-1}	5 / 4 / 1
$L_{2-10\ \mathrm{keV}} > 10^{42}$ erg s^{-1} & Optical spectra-selected AGNs	18 / 11 / 7
$P_{1.4\ \mathrm{GHz}} > 10^{24}$ W Hz^{-1} & Optical spectra-selected AGNs	0 / 0 / 0
$L_{2-10\ \mathrm{keV}} > 10^{42}$ erg s^{-1} & $P_{1.4\ \mathrm{GHz}} > 10^{24}$ W Hz^{-1} & Optical spectra-selected AGNs	0 / 0 / 0

powers of these two AGNs are not known). The GOODS-N contains 50 optical spectra-selected AGNs at $0.2 < z < 1.2$, of which 13 are LINERs, 16 are Seyfert galaxies, and 21 have ambiguous AGN classifications.

2.2.4 AGNs Selected by Multiple Methods

Table 2.2.4 presents the numbers of X-ray-selected AGNs, high-power radio sources, and optical spectra-selected AGNs that have been identified in the AEGIS and the GOODS-N at $0.2 < z < 1.2$. Various characteristics of the corresponding host galaxies, including morphologies and colors, will be discussed in Chapters 5 and 6. Table 2.2.4 also provides the number of objects that have been identified by multiple methods, such as AGNs selected by both X-ray and optical spectra techniques.

It is clear from this table that there is not a strong overlap between the various samples, emphasizing the importance of utilizing multiple selection methods. For ex-

ample, fewer than 20% of the optical spectra-selected AGNs are also identified as AGNs because of their X-ray luminosities. One possible reason for the differences between the samples has been mentioned already – obscuration of the nuclear regions. Additional explanations include the redshift and color biases caused by the optical spectra selection technique. However, it is not fully understood why there is such a large discrepancy between the radio and X-ray selection techniques, and a full exploration of this is beyond the scope of the present work.

Chapter 3

Classifying Galaxy Morphologies

This chapter describes several of the techniques that have been implemented to morphologically classify galaxies from the AEGIS and GOODS-N regions. Combining the available techniques with the high spatial resolution *HST*/ACS images allows reliable morphology measurements out to high redshifts, which is necessary for the study of galaxies at $z \sim 1$.

Galaxy morphologies depend upon the rest-frame wavelengths of the images analyzed. At any given redshift, the observed wavelengths that correspond to the rest-frame B band are highly sensitive to recent star formation and thus provide an accurate representation of the current galaxy morphology. In contrast, redder rest-frame colors correspond to older stellar populations and may miss indications of recent activity. This distinction is particularly relevent for detection of recent or on-going galaxy interactions. At the specific redshifts ($0.2 < z < 1.2$) used for the analyses described here, the rest-frame B-band light approximately corresponds to the observed V-band images for

redshifts $0.2 < z < 0.6$ and to the observed I/i-band images for redshifts $0.6 < z < 1.2$. Therefore, the galaxy morphologies presented are based on the *HST*/ACS V- and I/i-band for galaxies at $0.2 < z < 0.6$ and $0.6 < z < 1.2$, respectively.

Code written by J. Lotz (e.g., Lotz et al. 2004) analyzes galaxy images and simultaneously measures the Gini coefficient G, the second order moment of the brightest 20% of a galaxy's flux M_{20}, concentration C, and asymmetry A. Concentration and asymmetry (Conselice 2003) have been widely used by many authors to describe AGN host galaxies (e.g., Grogin et al. 2003, 2005), facilitating comparisons between the results presented here and previous work. Lotz et al. (2004, 2008a) reported that G and M_{20} form a morphological galaxy classification system that is particularly sensitive to interacting galaxies and is reliable to redshifts $z \sim 1$. In addition, Lotz et al. (2008b) have shown that A and G may be more effective than C and A at separating interacting galaxies from non-interacting galaxies. The light profiles of AEGIS galaxies have been measured by R. Griffith (in preparation), using the GALFIT program (Peng et al. 2002) to determine Sérsic indices. Also, the incidence of kinematic close pairs has been determined by Lin et al. (2004, 2007).

3.1 G, M_{20}, C, and A

3.1.1 The Gini Coefficient

Abraham et al. (2003) were the first to use G (also an economic statistic used to characterize the distribution of wealth in a society) to describe the distribution of

light among the pixels associated with a galaxy. Pixel associations are determined from segmentation maps of each individual galaxy created by SExtractor (Bertin & Arnouts 1996). If n is the number of pixels assigned to a galaxy and f_i represents the flux from pixel i (ordered such that f_i increases with the pixel index), then we can use the methods described by Lotz et al. (2004, 2008a) and measure G using

$$G = \frac{1}{|\overline{f}|n(n-1)} \sum_{i}^{n} (2i - n - 1)|f_i|. \tag{3.1}$$

High values of G correspond to galaxies in which the light is distributed among a small fraction of the associated pixels, such as a galaxy featuring a single bright nucleus or for a galaxy that features multiple bright nuclei; this latter characteristic contributes to the greater sensitivity to interacting galaxies associated with G-M_{20} and G-A classifications. Low values of G correspond to a homogenous distribution of light among the galaxy's pixels, such as would be found for a smooth disk galaxy. Gini measurements of $0.3 < G < 0.7$ are common for observed galaxies.

3.1.2 M_{20}

The value of M_{20} depends on the spatial distribution of the light in a galaxy, relative to the center of the galaxy. Lotz et al. (2004) defined M_{20} as follows:

$$M_{20} \equiv \log_{10}\left(\frac{\sum_i M_i}{M_{\rm tot}}\right), \text{ while } \sum_i f_i < 0.2 f_{\rm tot}, \tag{3.2}$$

where

$$M_{\rm tot} = \sum_{i}^{n} M_i = \sum_{i}^{n} f_i[(x_i - x_c)^2 + (y_i - y_c)^2], \tag{3.3}$$

and $(x_c,\ y_c)$ is the galaxy center, as determined by minimizing $M_{\rm tot}$. The presence of multiple bright nuclei that are spatially separated from a galaxy's center increases the value of M_{20} toward -1.0. However, if the brightest 20% of the galaxy's light is positioned very close to the galactic center, as would be the case for an undisturbed elliptical galaxy, the value of M_{20} approaches -2.5 or -3.0. Typical observed galaxies have $-0.5 > M_{20} > -2.5$.

3.1.3 Concentration

Concentration C compares the radius enclosing a large fraction of a galaxy's flux to the radius enclosing a smaller fraction of its flux. For this work, we used the following definition, provided by Conselice (2003):

$$C = 5 \times \log(r_{80\%}/r_{20\%}), \tag{3.4}$$

where $r_{\rm n\%}$ represents the radius enclosing n% of the galaxy's flux. High values of C correspond to highly concentrated systems, such as elliptical galaxies, and the value of C decreases for more diffuse galaxies, generally including disk galaxies and many interacting systems. Concentrations $2 < C < 5$ are typical values for observed galaxies.

3.1.4 Asymmetry

Measuring the asymmetry A of a galaxy is a three-step process, beginning with a rotation of the galaxy image by 180° about its central axis. Then, the rotated image is subtracted from the original image, and finally, the sum of the absolute value of the residual flux is compared to the flux of the original galaxy (Conselice 2003). Highly

symmetrical galaxies, such as undisturbed ellipticals or disks, leave minimal residuals, and A is small; the significant residuals of disturbed and irregular galaxies correspond to higher values of A. Galaxies with $0 < A < 1$ are typical.

3.1.5 Reliability Criteria for G, M_{20}, C, and A

G, M_{20}, and C are considered reliable for galaxies that have $\langle S/N \rangle$ per pixel ≥ 2.5, elliptical Petrosian radii $r_{ell} \geq 0.3''$, and contiguous segmentation maps (as determined by SExtractor; Lotz et al. 2004, 2008a). Reliability criteria for measurements of A differ only in that the $\langle S/N \rangle$ per pixel must exceed 4.0, instead of 2.5.

3.1.6 Definitions of Morphology Classifications

Based on calibrations using more than 200 low-redshift galaxies, Lotz et al. (2004) found that the sensitivity of both G and M_{20} to multiple nuclei makes this classification technique particularly well suited for identifying interacting galaxies. They also defined three morphology classifications for the non-interacting galaxies. Lotz et al. (2008a) refined the interacting and non-interacting classifications, and we used these more recent classifications, defined as follows:

$$\text{Interacting} : G > -0.14\ M_{20} + 0.33, \tag{3.5}$$

$$\text{E/S0/Sa} : G < -0.14\ M_{20} + 0.33 \ \text{ and } \ G > 0.14\ M_{20} + 0.80, \tag{3.6}$$

$$\text{Sb} - \text{Ir} : G < -0.14\ M_{20} + 0.33 \ \text{ and } \ G < 0.14\ M_{20} + 0.80. \tag{3.7}$$

Pairing A with G allows the classification of galaxies as either interacting

or non-interacting (Lotz et al. 2008a). The current work implements the following definitions of interacting galaxies and non-interacting galaxies, similar to those used by Lotz et al. (2008a):

$$\text{Interacting} : G > -0.4\ A + 0.66 \quad \text{or} \quad A > 0.35 \quad \text{and} \tag{3.8}$$

$$\text{Non} - \text{interacting} : G < -0.4\ A + 0.66 \quad \text{and} \quad A < 0.35. \tag{3.9}$$

A combination of C and A form a third method that can be used to morphologically classify galaxies. Adopting the definitions suggested by Conselice (2003), the subset of AEGIS and GOODS-N galaxies that meet the higher $\langle S/N \rangle$ per pixel value are classified as interacting, early-type, or late-type as follows:

$$\text{Interacting} : A > 0.35, \tag{3.10}$$

$$\text{Early} - \text{type} : A < 0.35 \quad \text{and} \quad C > 3.5, \quad \text{and} \tag{3.11}$$

$$\text{Late} - \text{type} : A < 0.35 \quad \text{and} \quad C < 3.5. \tag{3.12}$$

3.2 Sérsic Profiles

The AEGIS galaxy images have been analyzed by R. Griffith (in preparation) using GALFIT Version 2.1c (Peng et al. 2002) to determine the Sérsic indices. The advantage of measuring the light profiles of the AEGIS galaxies is the potentially clearer distinction between galaxies that feature a single bright nucleus and systems exhibiting multiple bright nuclei; G tends to group such systems into similar categories. GALFIT can perform multi-component fits using profiles such as de Vaucouleurs, Sérsic,

exponential, and a stellar PSF; the AEGIS galaxies were analyzed using a Sérsic profile and a stellar PSF. R. Griffith (in preparation) used the following SExtractor outputs as initial guesses for GALFIT: mag=`MAG_BEST`, $r_e = 0.162 \times$ `FLUX_RADIUS`$^{1.87}$, and $b/a = 1 -$ `ELLIPTICITY`, following Häussler et al. (2007; see their Table 3), and $n = 2.5$ as an initial guess for the Sérsic index. Reliable GALFIT results are selected by requiring relative uncertainties of less than 15% of the effective radii and the Sérsic indices ($\Delta r_e \leq 0.15 \times r_e$ and $\Delta n \leq 0.15 \times n$), GALFIT magnitudes and SExtractor magnitudes agreeing to within 1.0 mag ($|m_{\rm GALFIT} - m_{\rm SExtractor}| \leq 1.0$), and Sérsic indices $0.2 < n < 8$ (R. Griffith, in preparation). Individual galaxies are classified as having disk-dominated, ambiguous, or bulge-dominated Sérsic profiles, corresponding to Sérsic indices $0.2 < n < 1.5$, $1.5 < n < 2.5$, and $2.5 < n < 8$, respectively.

3.3 Kinematic Close Pairs

The sample of kinematic close pairs (e.g., Patton et al. 2002), drawn from those galaxies that have high quality spectroscopic redshifts (Chapter 2), were identified by Lin et al. (2004, 2007) who required $\Delta V \leq 2$ for objects at $0.2 < z < 0.6$, $\Delta I \leq 2$ for objects at $0.6 \leq z < 1.2$, and a projected line of sight velocity $\Delta r_P \leq 50 h^{-1}$ kpc for objects at all redshifts (e.g., Patton et al. 2002, Lin et al. 2004). The number of identified pairs is a lower limit because some companions may be missed due to the incompleteness of the spectroscopic sample. For example, the spectroscopic redshift sampling rate in the AEGIS among neighbors of AGN hosts is 0.48 ± 0.13, compared

to 0.66 ± 0.02 among neighbors of galaxies without AGNs (where neighbors are defined as systems with separation $< 10.0''$, $\Delta V \leq 2$, and $\Delta I \leq 2$.) The lower sampling rate around AGN host galaxies indicates that the differences discussed in Chapter 5 may represent lower limits.

Chapter 4

The Effects of an AGN on Galaxy Color and Morphology Measurements

4.1 Introduction

Much of the current work relies on a variety of measurements to facilitate the characterization of AGN host galaxies. The morphology measurements have been meticulously calibrated using large samples of local and distant galaxies (e.g., Lotz et al. 2004), and Kauffmann et al. (2007) reported that the amount of AGN light that may contaminate the measured UV-optical color should be minimal. Seeking to more fully understand the effect of an AGN on the techniques used here, this chapter presents an examination of the extent to which an active nucleus may affect measurements of G, M_{20}, C, A, the Sérsic index, and the UV-optical color $NUV - R$.

The investigation consisted of two independent experiments. The first involved

the addition of a series of optical point sources to a sample of AEGIS galaxies; the point sources were scaled to contribute a specified fraction of the total flux coming from the resulting galaxy-AGN systems. Morphologies of the simulated systems were then measured and compared to the measured morphologies of the original systems. A similar experiment was recently performed by Simmons & Urry (2008), who studied the effect of an AGN (also represented by a point source) on measurements of the Sérsic index; they found that the its reliability depends on the number of components used during the fitting (cf. § 3.2).

For the second experiment, a quasar spectral energy distribution (SED) was added to the SEDs of quiescent galaxies to determine how an AGN affects the UV-optical colors of its host galaxy. As for the first experiment, the quasar SED was scaled to contribute a set of specified fractions of the total flux coming from the final galaxy-AGN systems, and then the colors of the original and final systems were measured and compared. Finally, the results of these two experiments were combined to more clearly illustrate the effect that an AGN might have on the observed color and morphology of its host galaxy.

4.2 Experiment #1: Adding a Point Source to a Galaxy

4.2.1 Data for Morphology Measurements

Galaxy morphologies indicate the history of the galaxy prior to observation, thereby providing a means of investigating potential AGN triggers. However, AGNs are

often visible as an apparent point source in the host galaxy, and occasionally nearly (or entirely) overwhelm the galaxy's observable light. The most prominent AGNs are easy to identify and flag as having potentially unreliable computer-determined morphologies. Unfortunately, the optical contributions from lower-strength AGNs, such as those associated with Type-2 Seyfert galaxies or LINERs, may subtly yet systematically contaminate morphology measurements, resulting in an inaccurate characterization of AGN host galaxies.

The galaxies used for this first experiment were drawn from the AEGIS region observed by the *HST*/ACS (§ 2.1.1), and they were chosen to represent a variety of initial morphologies in order to thoroughly investigate the effect of an AGN on the morphology measurements. Galaxies with X-ray luminosities $L_{2-10\ \mathrm{keV}} > 10^{42}$ erg s^{-1}, radio powers $P_{1.4\ \mathrm{GHz}} > 10^{24}$ W Hz^{-1}, and/or identified optical spectra-selected AGNs (§ 2.2) were excluded from the sample so that the effect of an AGN could be methodically controlled. As mentioned in § 2.1.1, the AEGIS region observed by the VLA does not completely encompass the *HST*/ACS-observed region. To avoid including any unidentified high-power radio sources, the selected galaxies were therefore required to be located in a region observed by the *HST*/ACS, *Chandra*, the DEEP2 Redshift Survey, *and* the VLA (§ 2.1.1). The galaxies were also required to have *spectroscopic* redshifts $0.2 < z < 0.6$, so that all the analyses could be performed using the V-band images, which approximately correspond to the rest-frame B band (cf. Chapter 3) at these redshifts.

A sample of galaxies meeting these criteria was created from two of the *HST*/ACS

tiles that contained the highest numbers of eligible galaxies, tiles 1403 (34 galaxies) and 1503 (28 galaxies). This sample of 62 galaxies was then refined by imposing the criteria designed to guarantee the reliability of the individual morphology measurements (§ 3). Because the morphology measurements, and combinations thereof, require different criteria, the final samples used for each morphology analysis differ slightly; descriptions of each sample are provided with the results.

Tiny Tim (Krist 1993) was used to determine an appropriate V-band point-spread function (PSF) for the AEGIS *HST*/ACS observations, and this PSF was then systematically added to the V-band galaxy images as a representation of an AGN. For the current work, the PSF was represented by a square array of 121 pixels × 121 pixels, designed to complement the size of postage stamps created from the original galaxy images. The PSF used while running GALFIT to determine the Sérsic profiles was the same PSF used by R. Griffith (in preparation) to analyze the AEGIS galaxies; this PSF was determined independently of the PSF added to the galaxies.

4.2.2 Visual Simulation of an AGN

After selecting the 62 inactive galaxies that constitute the initial sample, the presence of an AGN was simulated in each of them by adding the PSF to each galaxy's V-band image. Taking the SExtractor value `MAG_BEST` as an approximation of the apparent magnitude of each galaxy, the V-band fluxes of each of the initial 62 galaxies ($f_{gal} = 10^{-0.4\times(\texttt{MAG\_BEST}-26.486)}$, where f_{gal} has units of [counts/s]) were calcluated. Then, the scaling factors necessary to cause the PSF to contribute a fraction N_{AGN} of

the total flux observed from the resulting galaxy-AGN system was determined, where $f_{AGN} = f_{gal} \times [n_{PSF}/(1n_{PSF})]$. Values of N_{AGN} ranged from 5% to 50%, and increased by 5% increments (N_{AGN} = 5%, 10%, 15%, etc.).

When a galaxy's natural position of maximum intensity (as defined by SExtractor's `X_PEAK` and `Y_PEAK`; Bertin & Arnouts 1996) is offset from the galaxy's geometrical center, increasing the brightness of the geometrical center may result in a galaxy image containing two bright nuclei. Although this could allow insightful tests of the morphology measurements, the current goal was to increase the intensity of the natural nucleus. Therefore, when the scaled PSFs were added to the galaxy images, the center of the PSF array was positioned to coincide with (`X_PEAK`, `Y_PEAK`) from the SExtractor measurements of the original galaxy images.

Although the original sample contained 62 inactive galaxies, application of the reliability criteria defined in Chapter 3 resulted in samples containing 57 galaxies for which measurements of G, M_{20}, and C are considered reliable, 52 galaxies for which Sérsic indices are considered reliable, and 47 galaxies for which A measurements are considered reliable. Therefore, results presented for G, M_{20}, or the combination of the two were based on the sample of 57 galaxies, results determined using the Sérsic index alone or combined with G were based on the sample of 52 galaxies, and the sample of 47 galaxies was used for analyses involving A, C, G-A, and C-A. The five galaxies meeting the $G/M_{20}/C$ criteria but not meeting the Sérsic criteria have $n = 0.2$ or $n = 8$. The 10 galaxies meeting the $G/M_{20}/C$ criteria but not meeting the A criteria have $3 < \langle S/N \rangle$ per pixel < 4.

4.2.3 The Effect of an AGN on Individual Morphology Measurements

Figures 4.1- 4.5 show the results from individual morphology measurements as a function of the fraction of rest-frame B band light contributed by the simulated AGNs. Specific details relevant to the results of each individual measurement are described below.

In each of these figures, the symbols indicate the change in the specified morphology measurement (e.g., $\Delta G = G_{\rm final} G_{\rm initial}$) as a function of $N_{\rm AGN}$ (the fraction of rest-frame B-band flux contributed by the simulated AGN). Black triangles represent systems initially classified as interacting galaxies; red circles represent systems initially classified by as E/S0/Sa, early-type, or non-interacting galaxies; and blue squares represent systems initially classified as Sb-Ir or late-type galaxies. Descriptions of the figures specify which morphology classification methods were used for the galaxies represented in the corresponding figures. Occasional "missing" symbols, such as in the second column and second row of Figure 4.1 (object 13017330), indicate that the system failed the necessary reliability criteria for the corresponding value(s) of $N_{\rm AGN}$. The solid curves connecting the symbols and the dashed line at, e.g., $\Delta G = 0$ serve to guide the eye. ID numbers of the original galaxies are shown at the top of each plot.

4.2.3.1 G

When a galaxy's nuclear flux significantly increases, the measurement of the distribution of light, G, would be expected to monotonically increase because more of the light would be distributed among fewer of the pixels associated with the galaxy.

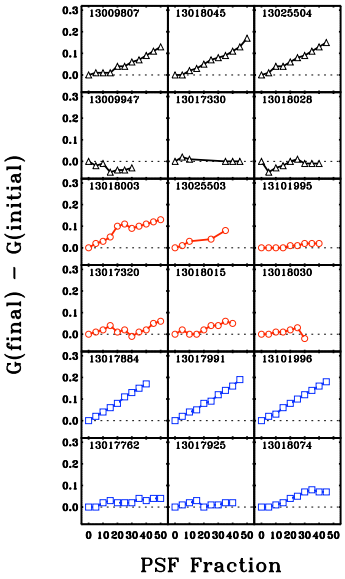

Figure 4.1: ΔG as a function of $N_{\rm AGN}$.

Figure 4.1 shows ΔG as a function of $N_{\rm AGN}$. The six rows are paired by initial morphology, as determined by G-M_{20} (§ 3.1). The first of each pair of rows shows examples of systems for which G generally behaves as expected, increasing as the fraction of light contributed by the AGN is increased, and the second row of each pair shows examples of unexpected cases for which $\Delta G \approx 0$ or G actually decreases.

G behaves as expected for a majority of the initially Sb-Ir galaxies; the examples shown represent most of the Sb-Ir galaxies for which G does not smoothly increase with AGN fraction. The initially interacting galaxies also have examples of smoothly increasing G, but they are less common among the sample, and there are a wider variety of unexpected results. E/S0/Sa galaxies tend to experience little change in the measured G, or else to change erratically.

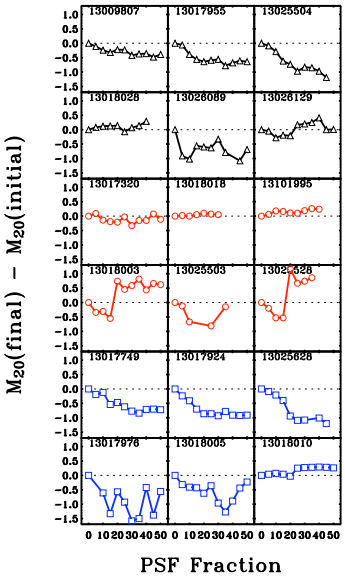

Figure 4.2: ΔM_{20} as a function of $N_{\rm AGN}$.

4.2.3.2 M_{20}

In contrast to the expected increase in G with AGN fraction, the value of M_{20} would be expected to *decrease* as the fraction of light contributed by an active nucleus increased. Increasing the brightness of a few adjacent pixels, such as the nuclear region of a galaxy, tends to decrease the spatial distribution of the brightest 20% of the pixels without changing the overall spatial distribution of the galaxy's pixels, thereby decreasing M_{20} relative to its initial value. Figure 4.2 shows ΔM_{20} as a function of $N_{\rm AGN}$, and the six rows are again paired by initial morphology determined by G-M_{20} with examples of expected results preceding examples of unexpected results.

The systems initially classified as interacting or Sb-Ir galaxies have several examples of expected behavior; in contrast the systems initially classified as E/S0/Sa

galaxies tend to experience minimal decreases in M_{20}, perhaps because they already have some of the lowest expected values of M_{20}, while the other two classifications include many systems beginning with high M_{20}. Examples of systems that do not behave as expected include cases in which M_{20} *increases* with $N_{\rm AGN}$ and cases for which the measurements seem to oscillate strongly, so that there is no clear pattern of increase or decrease.

4.2.3.3 C

The version of concentration used for the current work (§ 3.1 is proportional to the negative log of the radius enclosing 20% of a galaxy's light (r_{20}) to the radius enclosing 80% of the light (r_{80}). Increasing the light coming from a few adjacent pixels will cause both radii to decrease, but r_{20} will be more significantly affected, and C would be expected to increase as the AGN fraction increases. However, as the AGN fraction approaches and exceeds 20%, r_{20} is effectively measuring the radius of the point source function, rendering measurements of C essentially meaningless for galaxies containing a very bright AGN. Figure 4.3 shows a few examples for which the galaxy's concentration smoothly decreases, such as 13025511 and 13026129, but most systems behave as expected, at least until the AGN fraction reaches 20%. Measurements from systems with larger AGN fractions are sometimes automatically excluded by failing to meet the necessary reliability criteria (e.g., 13018058) and sometimes behave erratically (e.g., 13016227). The initial morphologies indicated in this figure were determined by the C-A method (§ 3.1).

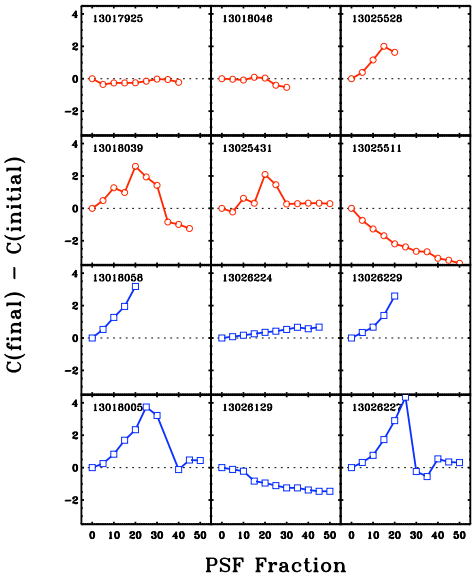

Figure 4.3: ΔC as a function of $N_{\rm AGN}$.

4.2.3.4 *A*

Asymmetry is not expected to be affected by the brightness of a central nucleus; increasing the brightness of the center will do nothing to alter the appearance of the majority of the galaxy. However, the location to which we added the simulated AGN was selected to coincide with the original location of the brightest spot in the galaxy (cf. § 4.2.2), and this location did not always fall in the center. As illustrated by Figure 4.4, the presence of an offset nucleus can significantly affect systems initially classified by *C*-*A* as late-type galaxies. Early-type galaxies seem to be less affected by the presence of an offset nucleus, but this result could also be caused a lower incidence of off-set nuclei among early-type galaxies. In general, the asymmetry of a galaxy is not significantly affected by the fraction of flux contributed by an AGN, unless the AGN is significantly

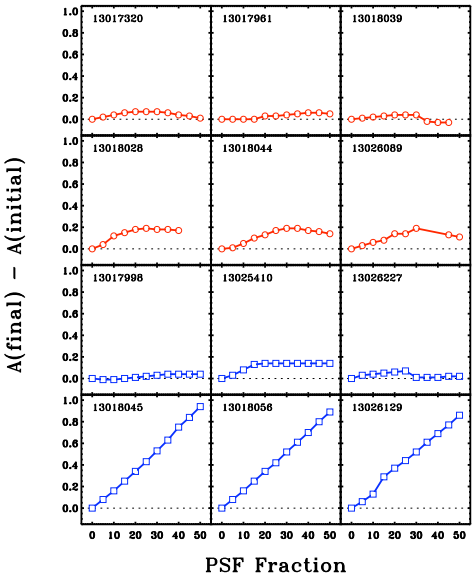

Figure 4.4: ΔA as a function of N_{AGN}.

offset from the galactic center.

4.2.3.5 Sérsic Index

The Sérsic index n is a measure of a galaxy's light profile, an indication of whether the galaxy is better represented as a disk ($n \approx 1$) or a bulge ($n \approx 4$). Hence, increasing the brightness of a few adjacent pixels would tend to increase the Sérsic index toward a bulge profile. Only one of the galaxies in our sample, the galaxy represented in Figure 4.5 with ID number 13018046, actually experienced a clear *decrease* in the Sérsic index as the AGN fraction was increased. Several systems experienced very little change, such as the galaxies with ID numbers 13018045, 13018003, and 13018010, independent of the initial morphology. The Sérsic indices of the remaining systems generally increased with the AGN fraction. The initial galaxy morphologies of the galaxies represented in

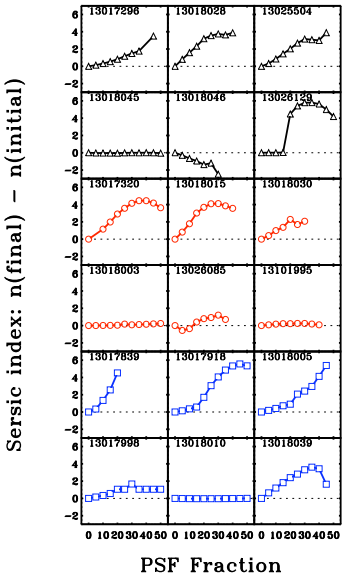

Figure 4.5: Δn as a function of $N_{\rm AGN}$.

Figure 4.5 were determined by G-M_{20}. The results from a two-component fit differed insignificantly from the results from a single-component fit; only the latter results are presented here.

4.2.4 Morphology Classification Methods

After determining the effect that the simulated AGN has on the individual morphology measurements, the next several figures (Figures 4.6- 4.9) illustrate how an AGN affects the morphology classifications of its host galaxy. The first panel in each of these figures graphically illustrates the two or three morphology classifications (as defined in Chapter 3) for the corresponding set of morphology measurements; these are represented by solid lines which are reproduced as dotted lines in the remaining panels.

The second panel, labeled "0%", shows the locations on the diagram of the initial galaxies, and the remaining four panels show the galaxy-AGN systems corresponding to the $N_{\rm AGN}$ indicated in the lower right-hand corner of the panel (10%, 20%, 30%, and 40%).

The shapes and colors of the symbols in each figure indicate the morphology classification of the initial galaxies, as shown by the "0%" panel, except for Figure 4.7, a plot of G vs. the Sérsic index; the initial morphologies indicated by the symbols in this figure are as determined by G-M_{20} (cf. Figure 4.6). These symbols are maintained throughout all the plots in this figure, so that one can observe the effect of an increasingly bright nucleus on galaxies of different morphologies. Only the galaxies that meet the reliabilty criteria for the morphology measurements shown (§ 3) are represented in any given panel, thus the number of symbols is not always constant from one panel to the next.

4.2.4.1 G-M_{20}

Results from the pairing of G with M_{20} are presented in Figure 4.6. As expected, an increase in the AGN fraction has the effect of increasing the measured Gini coefficient; this is especially noticeable among Sb-Ir galaxies and the interacting galaxies that have $M_{20} > -1.5$. It is also clear that AGN fractions $N_{\rm AGN} > 30\%$ can cause a significant decrease in the number of objects meeting the reliability criteria. For $N_{\rm AGN} = 50\%$, less than half of the initial sample continues to meet the reliability criteria, and a significant decrease in the measured elliptical Petrosian radius is almost

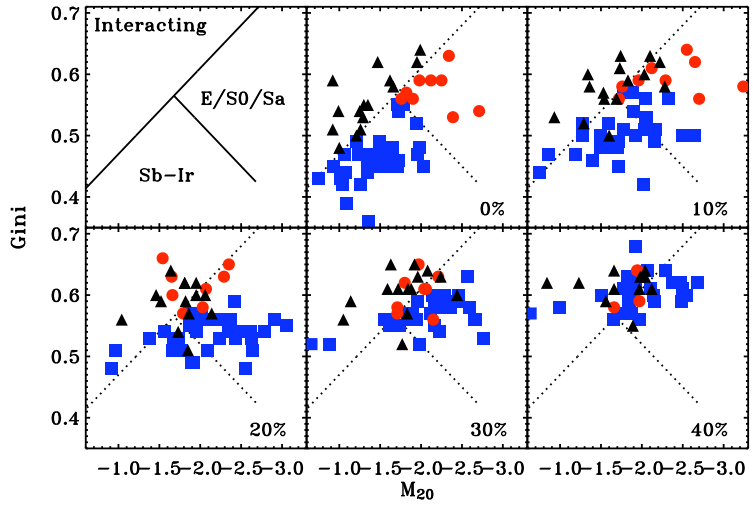

Figure 4.6: G-M_{20} diagrams of simulated AGN host galaxies.

always the cause of exclusion. One of the galaxies that failed to meet the reliability criteria at $N_{\rm AGN} = 50\%$, initially classified as an interacting galaxy, also failed the S/N and contiguity criteria.

There is also a trend for M_{20} to decrease as $N_{\rm AGN}$ increases. Sb-Ir galaxies are significantly affected by the presence of an AGN, even at $N_{\rm AGN} \sim 20\%$, and many could be mis-classified as E/S0/Sa galaxies by automated methods. The effect on E/S0/Sa and interacting galaxies is less significant, but there is still concern that up to 50% of such galaxies would be mis-classified for strong AGNs.

4.2.4.2 G- Sérsic index

Figure 4.7 depicts the pairing of G and the Sérsic index n. The Sérsic indices indicated in this figure were determined using a single-component fit (the Sérsic profile;

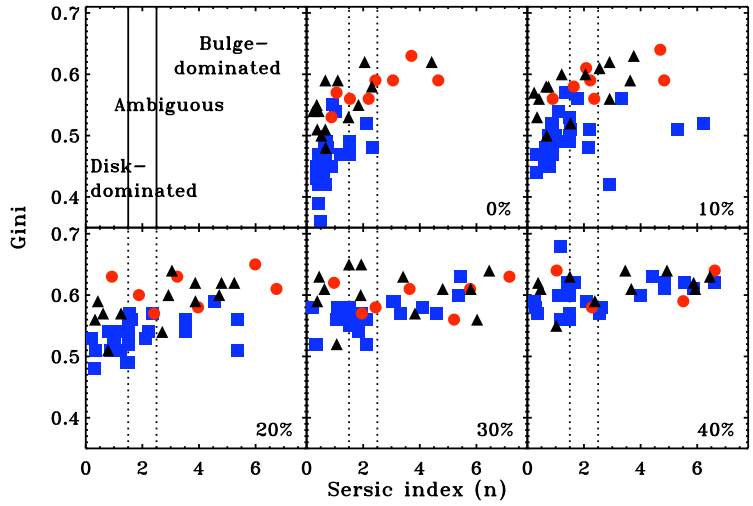

Figure 4.7: G- Sérsic index diagrams of simulated AGN host galaxies.

cf. § 3.2). Of the 52 initial galaxies that meet the required criteria, less than half continue to meet the criteria when $N_{\rm AGN} = 50\%$. Most of the galaxies that do *not* meet the criteria fail the size criterion (i.e., they have $r_{\rm Ell} < 0.3''$); one galaxy also fails the S/N and the contiguity criteria (this is the same galaxy mentioned in § 4.2.4.1 which was initially classified as an interacting galaxy by G-M_{20}).

AGNs most significantly affect the Sérsic profiles of systems initially classified as Sb-Ir galaxies, but the effect does not seem quite as drastic as the it does on the G-M_{20} classification. As the AGN fraction increases, about half of the systems initially classified as Sb-Ir galaxies transition from disk-dominated or ambiguous classifications into bulge-dominated classifications. Many of the Sérsic profiles of systems initially classified as E/S0/Sa or interacting galaxies become more firmly bulge-dominated, but

there are also several objects of all initial morphologies for which the Sérsic index undergoes an inconsequential amount of change as the AGN fraction increases.

As was shown by the previous figure, the addition of a point source tends to increase the value of G so that although the galaxy sample initially has a large range of G values, the final range (as $N_{\rm AGN}$ approaches 40%-50%) is rather narrow. The Sérsic index also tends to increase as the fraction of light coming from an added point source is increased, but this pattern does not apply to all galaxies, as indicated by the wide spread in Sérsic indices at high point source fractions. This suggests that G is more sensitive than the Sérsic index to the presence of a point source in a galaxy. As $N_{\rm AGN}$ and n increase, some of the galaxies originally classified as disk-dominated are instead classified as bulge-dominated galaxies, suggesting that the fraction of AGN host galaxies that are classified as disk-dominated should be considered a lower limit to the true fraction of disk-dominated AGN hosts. Similarly, the fraction of AGN host galaxies classified as bulge-dominated should be considered an upper limit.

One of the advantages of indicating the G-M_{20} classifications on this figure, in particular the panel representing a 0% AGN fraction, is that it shows that systems initially classified as interacting or Sb-Ir galaxies are generally classifed as disk-dominated or ambiguous, but only about half of the E/S0/Sa galaxies are classified as bulge-dominated, and some are actually classified as disk-dominated. Comparing the G-M_{20} morphology to the Sérsic index suggests that the Sérsic index may not provide a clear separation between Sb-Ir galaxies and E/S0/Sa galaxies. This apparent inconsistency needs more careful consideration.

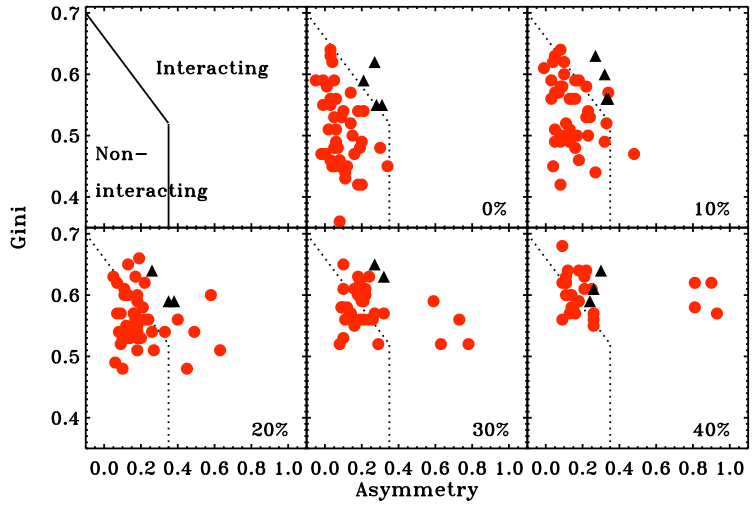

Figure 4.8: *G*-*A* diagrams of simulated AGN host galaxies.

4.2.4.3 *G*-*A*

The third analysis using G pairs it with A, as shown in Figure 4.8. Unless the AGN was simulated at a location significantly offset from the geometrical center of a galaxy, the change in A due to the simulated AGN was effectively null. Four of the initially non-interacting galaxies steadily increased their measured A as the AGN fraction increased, but the asymmetries of the majority of the galaxies remainied nearly constant. As shown previously, a the Gini coefficient of a galaxy steadily increases with $N_{\rm AGN}$ (cf. Figure 4.6 and Figure 4.7).

Among galaxies initially classified as interacting by the *G*-*A* method, there is little change in the measured values of G and A as the fraction of light coming from the point source increases. However, as $N_{\rm AGN}$ increases, the region indicating inter-

action suffers from contamination by misclassified non-interacting galaxies. Figure 4.8 also shows that the sample of galaxies classified as non-interacting is consistently pure, though increasingly incomplete as $N_{\rm AGN}$ increases. This may indicate that the fraction of AGN hosts identified as interacting represents an upper limit, and the fraction of AGN host galaxies identified as non-interacting should be considered a lower limit.

With the increase in AGN fraction, the number of galaxies meeting the reliabilty criteria steadily decreases; $\sim 40\%$ of the original sample have $r_{\rm Ell} < 0.3''$ when $N_{\rm AGN} = 40\%$. In addition, one galaxy also fails the S/N and the contiguity criteria (this is the same galaxy mentioned in § 4.2.4.1; it is initially classified as an interacting galaxy by G-A).

4.2.4.4 C-A

Figure 4.9 shows the results of morphology classifications based on C and A. It is again clear that A does not significantly change for the majority of the galaxies in the sample; the few objects for which a significant change is observed are those for which the simulated AGNs did not coincide with the galactic center (cf. § 4.2.4.3). Increasing the AGN fraction generally causes an expected increase in C, but many of the systems initially classified as late-type galaxies retain their classifications. However, as discussed previously (§ 4.2.3.3), concentration measurements should only be reliable to $N_{\rm AGN} = 20\%$, otherwise the concentration is effectively a measurement of the PSF that was added to the initial system.

The C-A classification method has the advantage that few of the early-type

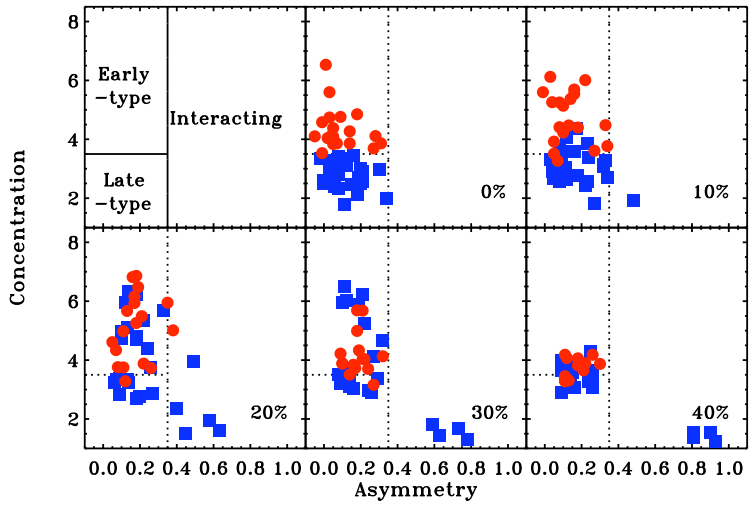

Figure 4.9: C-A diagrams of simulated AGN host galaxies.

galaxies are incorrectly classified as the AGN fraction increases. However, the early-type classification becomes significantly contaminated with late-type galaxies, and approximately 40% of the initial galaxies are excluded for large $N_{\rm AGN}$, again mainly due to the size criterion. In addition, one galaxy also fails the S/N and the contiguity criteria (this is the same galaxy mentioned in § 4.2.4.1; it is initially classified as a late-type galaxy by C-A). To summarize, for AGN hosts, the early-type classification is rather complete, but impure, while the late-type classification is mostly pure, but incomplete; the interacting classification is generally pure and expected to be complete.

4.3 Experiment #2: Adding AGN Spectral Templates to Quiescent Galaxy Spectral Templates

For the second experiment, an investigation of the effect of an AGN on the measured UV-optical color of its host galaxy, a spectral template representing a quasar was added to spectral templates representing three inactive galaxies — an elliptical, an Sb galaxy, and an Sc galaxy. The quasar template was scaled to contribute specified fractions of the rest-frame B-band flux of the resulting galaxy-AGN systems, consistent with the method used for the first experiment (§ 4.2). The spectral templates and the methods used for this experiment are presented in detail below. The goal of this experiment was to determine the fraction of the total flux contributed by an AGN that was necessary to move a red sequence or green valley galaxy (further) into the green valley or the blue cloud and to later compare the morphology of the analyzed systems to the morphologies of AGN host galaxies commonly found in the $NUV - r$ green valley and blue cloud.

4.3.1 Quiescent Galaxy Templates

Kinney et al. (1996) presented spectral templates of several galaxy types — including elliptical, Sb, and Sc galaxies — based on observations using the *International Ultraviolet Explorer* (*IUE*), the Cerro Tololo Inter-American Observatory (CTIO), and the Kitt Peak National Observatory (KPNO). At wavelengths 1200-3200Å, the *IUE* observed 200 arcsec^2 at the center of each galaxy, and the resulting spectra have a

resolution of $\approx$ 6Å. At the CTIO, the Frutti detector on the 1-m telescope gathered spectra for visible wavelengths, and the CCD detector on the 1.5-m telescope was used to observe near-IR wavelengths. Optical spectra observed at the CTIO were measured with slits $10'' \times 20''$, designed to match the area of the *IUE* aperture. The Reticon spectrograph at KPNO was used to obtain the optical spectra for the Sc galaxy template used here; the spectrograph has a 10-Å resolution, a $13.5''$-diameter circular aperature, and a wavelength coverage of 3200-7700Å (McQuade et al. 1995; Kinney et al. 1996).

Table 1 of Kinney et al. (1996) lists properties of the individual galaxies observed, and their Table 2 specifies which galaxies were used for each template. The elliptical template is based on UV and optical spectra from NGC galaxies 1399, 1404, 6868, and 7169. For the Sb template, Kinney et al. (1996) combined UV spectra from NGC galaxies 210, 2841, 4102, 4826, and 7083; optical spectra were available for only two of these galaxies (NGC 210 and NGC 7083). The Sc template is based on NGC galaxies 598, 1058, 1637, 2403, 3432, 3994, 4259, and 5194; optical spectra were only available for NGC 598 and NGC 2403.

To create the spectral templates, Kinney et al. (1996) shifted each spectrum to its rest frame, corrected for any Galactic exitinction, and then averaged the UV and optical spectra within each galaxy morphology group (e.g., Sc). Optical spectra were averaged separately from UV spectra, but similar methods were employed for both averaging processes, and then the two averaged spectra were combined to produce the final templates. Kinney et al. (1996) compared their quiescent galaxy templates to results from Kennicutt (1992) and noted that their Sb template does not sufficiently

represent young stellar populations in the disk. This suggests that colors derived from the Sb galaxy template may be too red. However, this did not adversely affect the work reported here.

4.3.2 Active Galaxy Templates

A quasar spectral template was prepared by Francis et al. (1991) as a composite of more than 700 individual quasar and AGN spectra from the Large Bright Quasar Survey (LBQS). Roughly 500 of the quasars and AGNs were observed using the MMT; the remainder were observed using the southern Du Pont Telescope at the Las Campanas Observatory. Both sets of observations included at least 3200-6800Å at a resolution of approximately 6Å and a S/N = 12. See the paper by Francis et al. (1991) for complete details of the preparation of the spectral template.

4.3.3 Spectroscopic Simulation of an AGN

Before adding the spectral templates described in SS 4.3.1 and 4.3.2, the rest-frame B-band flux from the quasar template was scaled to contribute specified fractions (5%, 10%, 15%, ... 50%) of the rest-frame B-band flux from the resulting galaxy+quasar spectra. After adding the scaled quasar spectrum to the galaxy spectra, the NUV$-r$ colors of each of the original and new systems was measured, and the fraction of light from the AGN spectra that moved a red sequence or green valley galaxy (further) into the green valley or blue cloud was determined. Varying the flux contribution from the quasar spectral template effectively simulated the addition of AGNs with a range of

luminosities.

Synphot[1], a package available for the Image Reduction and Analysis Facility[2] (IRAF) includes a task named `calcphot` that measures the flux f_ν [erg s^{-1} cm^{-2} Hz^{-1}] in a specified passband for an input spectrum. Using this task we measured f_ν for the *GALEX* NUV, SDSS r, and Johnson B passbands from each of the spectral templates. Scaling of the AGN templates with respect to the quiescent galaxy templates was based on the B passband fluxes measured from each spectral template as follows:

$$\mathrm{NUV}_{system} = \mathrm{NUV}_{\mathrm{galaxy}} + (\mathrm{NUV}_{\mathrm{AGN}} \times B_{galaxy}/B_{AGN}) \times [n/(1n)]/\mathrm{and} \tag{4.1}$$

$$r_{system} = r_{\mathrm{galaxy}} + (r_{\mathrm{AGN}} \times B_{galaxy}/B_{AGN}) \times [n/(1n)]; \tag{4.2}$$

n represents the specified fraction of the total B band flux contributed by the AGN spectral template; $B_{\mathrm{system/galaxy/AGN}}$ represents the B band flux contributed by the combined system, the galaxy, or the AGN; $\mathrm{NUV}_{\mathrm{system/galaxy/AGN}}$ represents the NUV flux contributed by the combined system, the galaxy, or the AGN; and $r_{\mathrm{system/galaxy/AGN}}$ represents the r band flux contributed by the combined system, the galaxy, or the AGN. The NUV$-r$ color was then calculated as follows:

$$\mathrm{NUV} - r = -2.5 \times \log(\mathrm{NUV}/r). \tag{4.3}$$

This method of calculating the color is equivalent to first converting the fluxes to AB magnitudes (e.g., NUV $= -2.5 \times \log(f_{\mathrm{NUV}})48.60$) and then calculating the difference between the NUV and r measurements.

[1]http://www.stsci.edu/resources/software_hardware/stsdas/synphot
[2]http://iraf.noao.edu/iraf-homepage.html

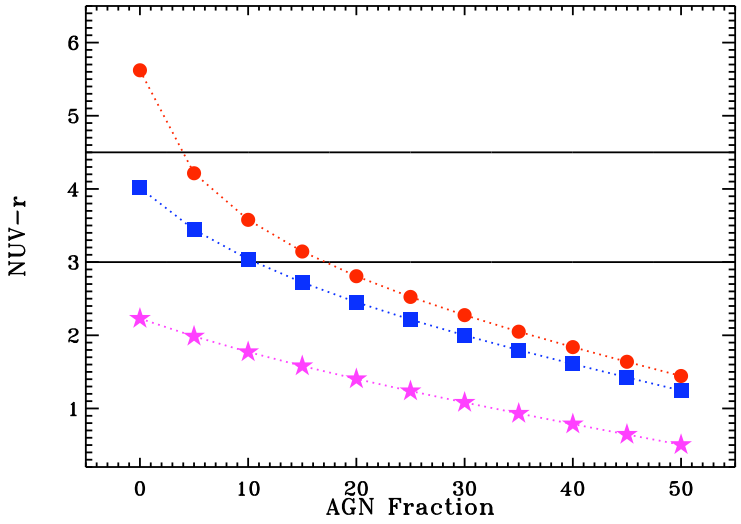

Figure 4.10: $NUV - r$ as a function of the fraction of B-band flux contributed by an AGN.

Figure 4.10 shows the change in $NUV - r$ color as a function of the fraction of B-band flux contributed by the quasar template. Red circles represent the elliptical template, blue squares represent the Sb template, and the magenta stars represent the Sc template; dotted lines connect the symbols to help guide the eye. The solid black lines mark the divisions between the $NUV - r$ red sequence, green valley, and blue cloud, as indicated in the figure and defined in § 2.1.1. The color of the systems resulting from the addition of the AGN and quiescent galaxy templates tend toward the color of the AGN as the AGN fraction increases.

The quasar template brings the initially red elliptical galaxy down into the green valley and then the blue cloud by AGN fractions of 5% and 20%, respectively. The Sb galaxy is also drawn from its initial location in the green valley down to the blue

cloud when only 10% of the B-band flux is contributed by the AGN. Although the color of the Sc galaxy is also affected by the quasar template, it was blue to begin with, so the effect is less signficant. This suggests that the UV-optical colors of AGN host galaxies may be more significantly affected by an active nucleus than previously believed (e.g., Kauffmann et al. 2007); however, Kauffmann et al. (2007) specifically excluded quasars, so this might be a result that depends very strongly on the type of AGN observed.

4.4 Observable results: UV-Optical Color vs. Sérsic Index

Figure 4.11 shows the color-morphology diagram created by matching the simulated UV-optical color ($NUV - r$) results to the Sérsic indices using the fraction of rest-frame B-band flux contributed by the AGN. The large colored symbols outlined in black represent the initial galaxies, and the matching solid lines connect the symbol representing the initial galaxy to smaller black symbols representing each successive simulated system, progressing as $N_{\rm AGN}$ increases. Small gray symbols represent AEGIS galaxies at $0.2 < z < 0.6$, and the 'x's represent AEGIS X-ray-selected AGNs at the same redshift. All of the AEGIS galaxies represented in this figure were required to meet the reliability criteria for $NUV - R$ and the Sérsic index (§ 3.2).

This figure suggests that AGN hosts with Sérsic indices $n > 4$ are simply a result of the presence of the AGN; these are truly bulge-dominated systems. Although the UV-optical color *appears* to be significantly affected by the presence of an AGN, it is evident from Figure 4.11 that there are few observed AGNs that have color-morphology

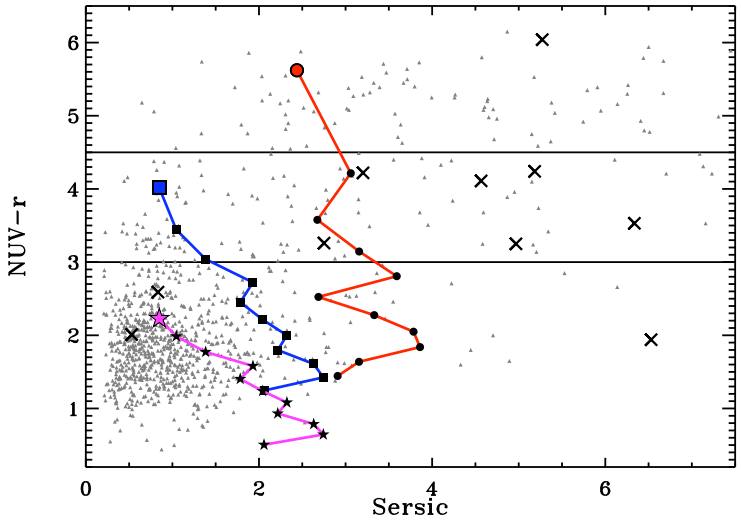

Figure 4.11: $NUV - r$ vs. Sérsic index of quiescent galaxies with AGNs added.

characteristics that are similar to those of the heavily contaminated systems. The simulated systems become very blue while maintaining low Sérsic indices, but the very blue *observed* AGN host galaxies have high Sérsic indices. Green valley AGN host galaxies that have Sérsic indices placing them in the ambiguous classification (§ 3.2) are the most likely to be incorrectly classified *and not easily identified as being problematic*, and thus extra caution should be taken when studying such systems.

Chapter 5

Morphologies of AGN Host Galaxies

5.1 Control Samples

Intrinsic properties (such as redshifts, stellar masses, and colors) of the AGN host galaxies discussed here differ slightly between the three samples, and they differ significantly from the majority of the AEGIS and GOODS-N galaxies observed at $0.2 < z < 1.2$. For example, AGNs from all three samples are hosted by galaxies that have masses $M_* > 2 \times 10^9\, M_\odot$, at least an order of magnitude more massive than the least massive galaxies detected in the AEGIS and GOODS-N. Comparing the morphological and color characteristics of our AGN host galaxy samples to a set of quiescent galaxies that have properties known to be highly inconsistent with typical AGN host galaxy properties will undoutedly, but unpredictably, bias the results. In an effort to minimize this bias, three control samples (corresponding to the three AGN samples) have been selected from among the AEGIS and GOODS-N galaxies.

Most of the AEGIS and GOODS-N galaxies at redshifts $0.2 < z < 1.2$ were initially eligible for inclusion in one or more of the control samples, but any galaxies known to host 5-σ X-ray or radio sources or an optical spectra-selected AGN were excluded. Then, for every AGN and high-power radio source in the AEGIS and GOODS-N, all of the galaxies from the same survey that had $|z_{\rm AGN} - z_{\rm Galaxy}| < 0.03$, B magnitudes $|M_{\rm B;\ AGN} - M_{\rm B;\ Galaxy}| < 0.4$, and colors $|(U-B)_{\rm AGN} - (U-B)_{\rm Galaxy}| < 0.1$ were selected as part of the control sample for that AGN. Thus, if four galaxies met the criteria for an AGN selected by both its radio power and its X-ray luminosity, those four galaxies became part of both the radio control sample and the X-ray control sample.

Table 5.1 provides the number of systems in each AGN sample and its corresponding control sample. In the results presented here, the morphology and color measurements of the AGN host galaxies are compared to the meausrements of the galaxies in the corresponding control samples, instead of to the full samples of AEGIS and GOODS-N galaxies at $0.2 < z < 1.2$.. For clarity, this chapter and the following chapter will refer to the "X-AGN", "X-control", "R-AGN", "R-control", "S-AGN", and "S-control" samples. Throughout *this* chapter, the X-AGN sample includes all AEGIS and GOODS-N galaxies that host an X-ray source with luminosity $L_{2-10\ \rm keV} > 10^{42}$ erg s^{-1}; the R-AGN sample includes all AEGIS and GOODS-N galaxies that host radio sources that with powers $P_{1.4\ \rm GHz} > 10^{24}$ W Hz^{-1}; the S-AGN sample includes all optical spectra-selected AGNs in the AEGIS and GOODS-N. The X-control, R-control, and S-control samples are the control samples corresponding to each of the AGN samples. In the *next* chapter, these terms will only refer to the AGN and control samples from

Table 5.1: Summary of control samples.

Sample	AGNs (#)	Control Sample (#)
X-AGN and X-control	186	1354
R-AGN and R-control	16	78
S-AGN and S-control	102	669

the AEGIS.

5.2 AGN Host Galaxy Morphologies

This section provides descriptions of the visual and measured morphologies of the AGN host galaxies; comparisons between galaxies in the AGN and control samples are also described. The figures presented in this chapter consist of four panels, each presenting a sub-sample of AEGIS and GOODS-N galaxies at $0.2 < z < 1.2$. In all four panels, red symbols represent GOODS-N galaxies, and blue symbols represent AEGIS galaxies; in panels (b)-(d), blue and red symbols represent AGN host galaxies, and gray symbols represent galaxies from the corresponding control samples. Solid lines shown in the figures represent divisions between morphology classifications, as defined in Chapter 3; the names of these classifications are shown in panel (a) of each figure. Symbols represent only those galaxies that meet the reliability criteria for the specified morphology measurements (see Chapter 3), so the number of symbols may change between figures.

Panel (a) shows the most general sample possible that meets the relevant criteria for the morphology measurements being presented. Symbols in panel (b) represent galaxies in the X-AGN and X-control samples, symbols in panel (c) represent galaxies

in the R-AGN and R-control samples, and symbols in panel (d) represent galaxies in the S-AGN and S-control samples. For panels (b)-(d), 'x's represent either X-ray-selected AGNs [panel (b)] or X-ray sources ($L_{2-10\ \mathrm{keV}} > 10^{40}$ erg s^{-1}) [panels (c) & (d)], open squares represent high-power radio sources ($P_{1.4\ \mathrm{GHz}} > 10^{24}$ W Hz^{-1}), and 'S's represent optical spectra-selected AGNs. Filled diamonds represent sources that are high-power radio sources, X-ray sources, *and* optical spectra-selected AGNs. An encircled symbol in panel (b) indicates that the AGN represented has an X-ray luminosity $L_{2-10\ \mathrm{keV}} > 10^{44}$ erg s^{-1}; in panel (c), circles mark radio-selected AGNs ($L_{1.4\ \mathrm{GHz}} > 10^{25}$ W Hz^{-1}).

5.2.1 X-ray-selected AGNs

X-ray-selected AGNs inhabit galaxies possessing a wide range of colors and morphologies. Several of the host galaxies appear "red and dead" with no obvious signs of interaction or nuclear activity, and many others are very clearly experiencing an interaction. However, undisturbed disk galaxies rarely host X-ray-selected AGNs; the few spiral galaxies in the X-AGN sample show evidence of recent disturbances, including highly asymmetric spiral arms, fragmented rings, and/or a potentially offset nucleus. Color images made by combining the AEGIS *HST* V and I band images show that most galaxies in the X-AGN sample are predominantly red, indicating a lack of recent star formation. However, there are several hosts that show evidence of current star formation. There is a stark contrast between the colors of X-ray sources with luminosities $L_{2-10\ \mathrm{keV}} > 10^{42}$ erg s^{-1} and those with luminosities $L_{2-10\ \mathrm{keV}} < 10^{42}$ erg s^{-1}; the former are as described above, but the latter, detected only at low redshifts, are

generally much bluer, consistent with the expectation that most of their X-ray emissions result from star formation. Several of the galaxies with the lower X-ray luminosities have what appears to be a visible point source, possibly due to nuclear starbursts.

Many of the most X-ray-luminous AEGIS AGNs ($L_{2-10\ \mathrm{keV}} > 2 \times 10^{43}$ erg s^{-1}) contain a clearly visible nuclear point source in the V and/or I band images, and the incidence of this seems to increase with X-ray luminosity. In contrast, few X-ray sources with luminosities $L_{2-10\ \mathrm{keV}} < 10^{42}$ erg s^{-1} contain an optically visible point source. When they are identifiable, the point sources are slightly more prevalent in galaxies that have some signs of disturbance, but they are also clearly evident in several undisturbed, red elliptical galaxies. Several of these galaxies are excluded from later analyses, probably due in part to the effects of the point source on morphological measurements.

Two of the X-ray-selected AGNs have radio powers $P_{1.4\ \mathrm{GHz}} > 10^{25}$ W Hz^{-1} (corresponding to radio-selected AGNs), and an additional 12 have powers $P_{1.4\ \mathrm{GHz}} > 10^{22}$ W Hz^{-1}. The two R-AGNs appear to be undisturbed, red elliptical galaxies at $z \approx 0.7$. Nuclear point sources are evident in six of the galaxies with lower-power radio sources. The wide range of galaxy characteristics evident among X-AGN galaxies is also evident when the sample is limited to X-AGNs that are also radio sources, with at least half of the sample showing some indication of interaction or disturbance. Eleven X-AGNs are also S-AGNs (two LINERs, seven Seyferts, and two broad-line AGNs that have very prominent nuclear point sources); three of these are also confirmed radio sources, though not R-AGNs. Only one of these shows strong evidence of a recent

interaction, although several of them have colors indicating some recent star formation, and most are elliptical or early-type disks.

Consistent with earlier work (Pierce et al. 2007), the distribution of X-AGN host galaxies on the G-M_{20} diagram differs from the distribution of X-control galaxies, especially with respect to the Gini coefficient. Panel (b) of Figure 5.1 shows this very clearly. The X-AGN galaxies tend to have values of G and M_{20} that place them in the E/S0/Sa (or "E-Sa") morphology classification, while the X-control galaxies extend to lower values of G. This conclusion, based upon inspection of the diagram, is supported by the results of Kolmogorov-Smirnov (K-S) tests (Fasano & Franceschini 1987) comparing the G and M_{20} distributions of the AGN and control samples. We found negligible ($<$0.01) probabilities that the G or M_{20} values of the X-control and X-AGN samples were drawn from the same parent population.

Considering the highest luminosity AGNs, those represented by circled symbols in Figure 5.1(b), it is found that such objects are rarely found in Sb-Ir hosts, as expected by the observed correlation between bulge mass and X-ray luminosity. More interestingly, it appear that most of these AGNs are either currently interacting or may have recently experienced an interaction, as suggested by the proximity to the dividing line between interacting and non-interacting galaxies. Inspection of the *HST* image of the GOODS-N AGN with $G < 0.3$ (and $L_{2-10\ \mathrm{keV}} = 10^{43}$ erg s^{-1} at $z = 1$) suggests that it may actually be an interacting galaxy.

Based on the G-M_{20} morphology classifications, we find that 17% of X-AGN galaxies are classified as interacting galaxies; this is to be compared to 11% of the X-

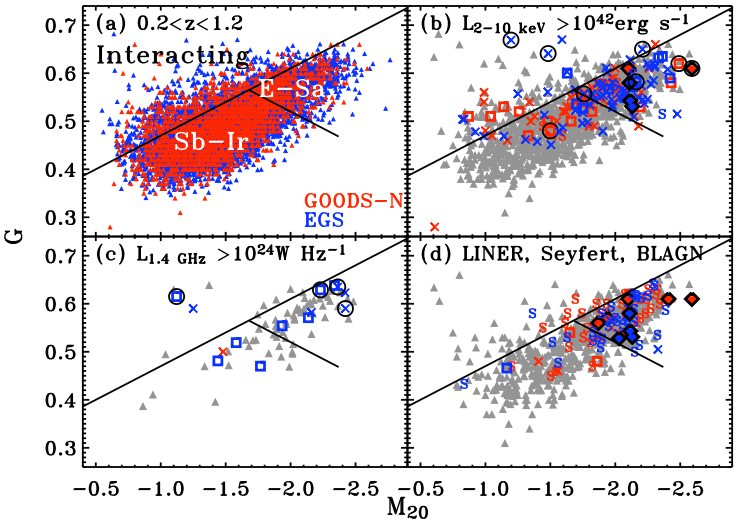

Figure 5.1: G-M_{20} diagrams of the control and AGN samples. Panels and symbols are as described in § 5.2.

control galaxies. Though these values are consistent within a 2-σ level of uncertainty, the differences between the fractions of galaxies classified as Sb-Ir and as E/S0/Sa is significant. Approximately half of X-AGN galaxies are classified as E/S0/Sa galaxies, while only a third of the X-control galaxies are classified as E/S0/Sa galaxies. Conversely, a third of the X-AGN galaxies and 58% of the X-control galaxies are classified as Sb-Ir galaxies. The fractions of AGN and control sample galaxies assigned to each of the various morphologies is summarized in Table 5.2.1.

Figures 5.2 and 5.3 show the distribution of galaxies in the AGN and control samples on the G-A and C-A diagrams, respectively. First recall that the higher $\langle S/N \rangle$ requirement causes the exclusion of several X-control galaxies with lower G measurements [cf. Figure 5.1(b) and Figure 5.2(b)]. The similarity between C measurements

Table 5.2: AGN host galaxy morphologies.

Sample	Sample Size	Mergers % (#)	E/S0/Sa % (#)	Sb-Ir % (#)
		G - M_{20}		
X-AGN	149	17^{+4}_{-3} (25)	52^{+7}_{-6} (78)	31±5 (46)
X-control	1128	11±1 (123)	31±2 (347)	58±2 (658)
R-AGN	14	14^{+19}_{-9} (2)	57^{+28}_{-20} (8)	29^{+23}_{-14} (4)
R-control	66	12^{+6}_{-4} (8)	58^{+11}_{-9} (38)	30^{+8}_{-7} (20)
S-AGN	91	7^{+4}_{-3} (6)	65^{+10}_{-8} (59)	29^{+7}_{-6} (26)
S-control	595	$8^{\pm}1$ (48)	42±3 (248)	50±3 (299)
		G - A		
X-AGN	106	8^{+4}_{-3} (8)	92^{+10}_{-9} (98)	...
X-control	718	$4^{\pm}1$ (26)	96±4 (692)	...
R-AGN	9	22^{+29}_{-14} (2)	78^{+42}_{-29} (7)	...
R-control	46	7^{+6}_{-4} (3)	93^{+17}_{-14} (43)	...
S-AGN	80	8^{+4}_{-3} (6)	93^{+12}_{-11} (74)	...
S-control	423	3^{+1}_{-1} (12)	97±5 (411)	...
		C - A		
X-AGN	106	3^{+3}_{-2} (3)	55^{+8}_{-7} (58)	42^{+7}_{-6} (45)
X-control	718	2^{+1}_{-0} (12)	31±2 (220)	68±3 (486)
R-AGN	9	11^{+26}_{-9} (1)	67^{+40}_{-26} (6)	22^{+29}_{-14} (2)
R-control	46	0^{+4}_{-0} (0)	61^{+14}_{-11} (28)	39^{+12}_{-9} (18)
S-AGN	80	4^{+4}_{-2} (3)	69^{+11}_{-9} (55)	23^{+7}_{-6} (22)
S-control	423	1±1 (5)	41±3 (174)	58±4 (244)

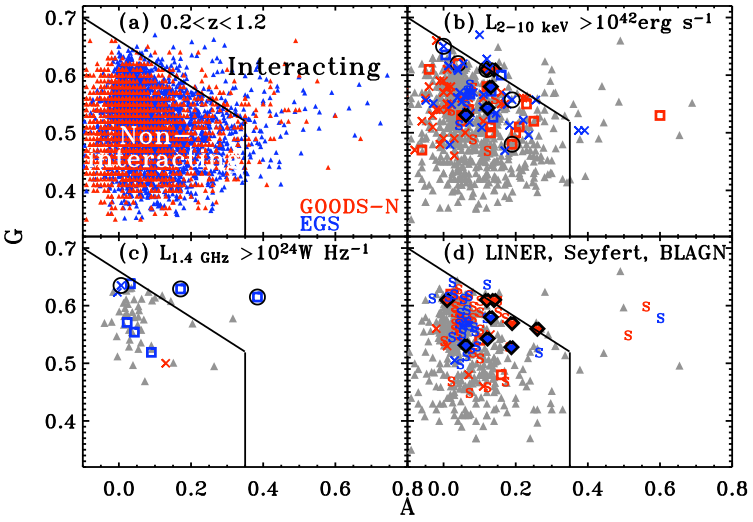

Figure 5.2: G-A diagrams of the control and AGN samples. Panels and symbols are as described in § 5.2.

of the X-AGN and X-control samples is very small, likely due to the few AGN hosts with very high concentrations ($C > 6$). However, the asymmetry measurements are statistically quite similar; a K-S test indicated a 72% probability that the two samples were drawn from the same parent population.

It is clear from these figures that the X-ray-selected AGNs are not classified as interacting at a significantly different rate than the galaxies comprising the X-ray control sample, though they are more concentrated. Interacting X-AGN galaxies make up 3% (C-A) to 8% (G-A) of the sample, and 2% (C-A) to 4% (G-A) of the X-control galaxies are so classified. The higher fractions of interacting galaxies from the G-A classification is a result of the finding by Lotz et al. (2008a) that galaxies with low values of A show signs of disturbance when they also have high values of G. Using the

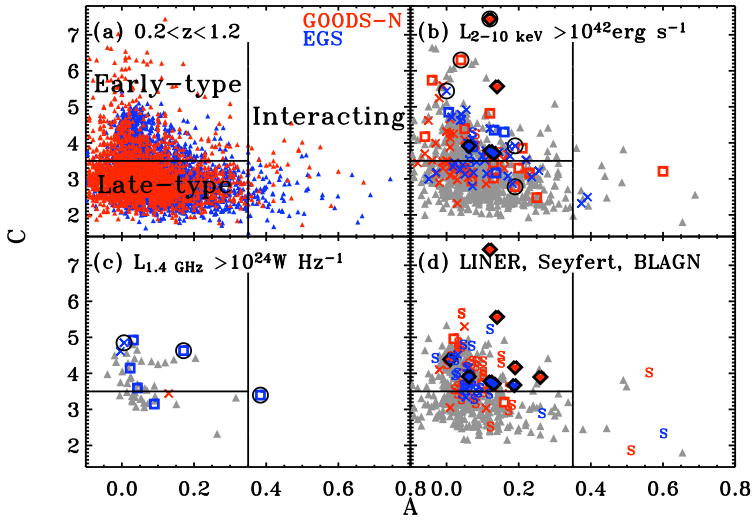

Figure 5.3: *C*-*A* diagrams of the control and AGN samples. Panels and symbols are as described in § 5.2.

C-based division between early-type and late-type galaxies (Figure 5.3), a significant difference is found between the fractions of X-AGN galaxies classified as early-type (55%) or late-type (42%) and the fractions of X-control galaxies classified as early-type (31%) and late-type (68%). These results are consistent with results from the G-M_{20} analysis.

Close kinematic companions are associated with 25% of the X-control galaxies and 25% of the X-AGN hosts (for both calculations, we limited the samples to include only those galaxies for which we have spectroscopic redshifts). Table 5.2.1 lists the number and fraction of AGN and control sample galaxies for which kinematic close pairs have been identified.

Table 5.3: AGN host galaxies with kinematic close pairs.

Sample	Sample Size	Pairs % (#)
X-AGN	96	25^{+6}_{-5} (24)
X-control	578	25±2 (143)
R-AGN	8	0^{+23}_{-0} (0)
R-control	37	19^{+10}_{-7} (7)
S-AGN	100	21^{+6}_{-5} (21)
S-control	293	31^{+4}_{-3} (91)

5.2.2 Radio-selected AGNs

The five radio-selected AGNs, all from the AEGIS, have three distinct types of host galaxies — two undisturbed, red elliptical galaxies, two with obvious signs of interaction, and one that appears to be a red disk with a faint nucleus and no bulge. The interacting and elliptical radio-selected AGN host galaxies have visible nuclear point sources, although the bright nucleus of the less powerful elliptical host may result from a nuclear starburst. The red disk has a small clump just off one end, suggesting interaction-related star formation. Radio sources with powers 10^{24} W Hz^{-1} $< P_{1.4\ \mathrm{GHz}} < 10^{25}$ W Hz^{-1} are similar to their higher-power counterparts in that most are predominantly red ellipticals, many of which show indications of interactions and star formation; one notable exception is a very clear merger at $z \approx 1.2$. Less powerful radio sources increasingly include disk galaxies, consistent with the expectation that star formation is the predominent source of radio emissions from such galaxies; however, there are also a few ellipticals and disturbed/irregular galaxies in the sample.

As mentioned above, there are two radio-selected AGNs that are also X-ray-selected AGNs; these are the two elliptical host galaxies. In addition, four radio sources

with 10^{24} W Hz^{-1} $< P_{1.4\ \mathrm{GHz}} < 10^{25}$ W Hz^{-1} are also X-ray sources (two have 10^{41} erg s^{-1} $< L_{2-10\ \mathrm{keV}} < 10^{42}$ erg s^{-1}, and two have $L_{2-10\ \mathrm{keV}} > 10^{42}$ erg s^{-1}). Two of the galaxies that host both a radio source and and X-ray source are potential dry mergers; a third galaxy is more of a train wreck. Six of the radio sources with 10^{22} W Hz^{-1} $< P_{1.4\ \mathrm{GHz}} < 10^{24}$ W Hz^{-1} are also identified as optical spectra-selected AGNs, and they are split roughly evenly between elliptical and disk host galaxies. One of the ellipticals shows evidence of a recent interaction, and two have bright nuclear point sources. Two of the disk galaxies are also X-ray-luminous ($L_{2-10\ \mathrm{keV}} < 10^{43}$ erg s^{-1}) and the third appears to have a significant amount of on-going star formation, along with an older stellar population.

The R-AGN sample is too small to provide statistically significant conclusions about the distributions of G and M_{20}, but there does seem to be a trend similar to the sample of X-ray-selected AGNs, in that more than half (57%) of the R-AGN galaxies are classified as E/S0/Sa, Sb-Ir classifications apply to a smaller fraction (29%), and interacting galaxies comprise the smallest fraction (14%). However, unlike the X-control galaxies, the R-control galaxies have a similar distribution of morphology classifications (interacting: 12%; E/S0/Sa: 58%; Sb-Ir: 30%). According to K-S tests, which support the apparent similarities between the G and M_{20} distributions of the R-AGN and R-control galaxies, the probabilities that the G and M_{20} measurements were made on galaxies drawn from the same parent population is 48% and 53%, respectively.

The most powerful radio-selected AGN ($L_{1.4\ \mathrm{GHz}} = 2.6 \times 10^{25}$ W Hz^{-1}) is classified as an E/S0/Sa by G-M_{20}, with $G = 0.59$; this classification is firmly supported

by visual inspections of the *HST* images. This source is also a luminous X-ray-selected AGN. The two radio-only AGNs show evidence of interactions; though only one is classified as an interacting galaxy by G-M_{20}, the other has measurements that place it very close to the division between interacting and non-interacting.

As with the X-ray samples, the higher $\langle S/N \rangle$ requirement used for measurements of A decreases the size of the samples that can be analyzed. Based on the asymmetry measurements, there is a high probability (78%) that the radio source and control samples were drawn from the same parent population. The concentrations are not quite as similar; a K-S test suggests an 18% probability that the two samples were drawn from the same parent population.

Figure 5.2(c) and Figure 5.3(c) indicates that R-AGN galaxies are slightly more likely to be classified as interacting (11% to 22%) than R-control galaxies (0% to 7%), though the fractions of galaxies classified as early-type (R-AGN: 67%; R-control: 61%) and late-type (r-AGN: 22%; R-control: 39%) by C-A are fairly consistent. What may be significant is the result that the *radio-selected AGNs* are more likely to be classified as interacting than the lower power radio sources included in these figures.

None of the eight (0%) R-AGN galaxies for which we have spectroscopic redshifts have a kinematically identified close companion. However, 19% of the R-control galaxies (also limited to the sub-sample for which we have spectroscopic redshifts) are identified as being part of a kinematic close pair. As with the X-ray sample, these fractions are roughly consistent.

5.2.3 Optical spectra-selected AGNs

On account of the method used to select the S-AGN sample, the vast majority of the host galaxies have red $U - B$ colors, and the *HST*/ACS images are generally consistent with the measured colors. There are several notable exceptions, especially at lower redshifts, where we find a higher fraction of Seyferts which appear to have more recent star formation. Nuclear point sources are apparent in a few of the LINERs and Seyferts, as well as in the BLAGNs. At least half of the S-AGN galaxies apparently undisturbed elliptical or early-type disks, and a few of the Seyfert host galaxies show well defined spiral structure. The remaining S-AGN galaxies could be classified as interacting or merger remnants, due to the presence of tidal features, rings, or asymmetric star formation structures.

Twelve of the S-AGN galaxies are also X-ray sources (eleven of which are X-ray-selected AGNs), and six of the S-AGN galaxies are also radio sources (though none are radio-selected AGNs); four are known to be both X-ray and radio sources, and three of the remaining X-ray sources are located in the region *not* covered by the radio survey. These galaxies have already been discussed above. The majority of S-AGN galaxies that are also X-ray or radio sources are Seyferts, but there are also two LINERs with high X-ray luminosities, in addition to the two BLAGNs. Both of these LINERs are hosted by apparently undisturbed elliptical galaxies, though the less X-ray-luminous of the two has a kinematically identified companion.

Optical spectra-selected AGNs fall between the two extremes represented by

the R-AGN and X-AGN galaxies, in that the distributions of G and M_{20} measurements of the AGN host and control sample galaxies are more similar than the X-ray samples, but not as similar as the radio samples. K-S tests suggest probabilities $\leq$0.01% that the S-AGN and S-control galaxies were drawn from the same parent population, based on measurements of M_{20} and G. Almost 7% of the S-AGN galaxies are classified as interacting, compared to 8% of the S-control galaxies. The fraction of S-control galaxies classified as E/S0/Sa and Sb-Ir are similar, 42% and 50%, respectively, but the corresponding fractions for the S-AGN galaxies show less consistency; 65% are classified as E/S0/Sa, and 29% are classified as Sb-Ir.

The probability that the asymmetries of the S-AGN and S-control galaxies were drawn from the same parent populations is 23%, according to a K-S test, but there is only a negligible probability that concentrations of the S-AGN and S-control galaxies were drawn from the same population. These statistics are not conclusive regarding whether or not the S-AGN and S-control galaxies were drawn from the same parent population.

According to Figures 5.2 and 5.3, 4% to 8% of S-AGN galaxies are classified as interacting, compared to 1% to 3% of the S-control galaxies. (Again, the higher fraction of interacting galaxies is associated with the G-A analysis.) The non-interacting S-control galaxies are more often classified as late-type (58%), while the S-AGN galaxies are more often classified as early-type (69%). These differences are roughly consistent with the inconclusive K-S tests reported earlier. There is a very evident division between "symmetric" and "asymmetric" galaxies in these samples. The two GOODS-N AGNs

with $A > 0.4$ have ambiguous AGN types; the third AGN, from the AEGIS, is classified as a LINER and is surrounded by at least three blue, star-forming objects.

The fractions of the optical spectra control and AGN samples that are associated with a kinematic close pair are less consistent; the fractions are 21% and 31%, respectively. See Table 5.2.1 for details.

5.3 Discussion

There are no AGNs actually selected as such by all three of our methods. Although many of the S-AGN galaxies have sufficiently high X-ray luminosities, they lack sufficient radio powers to be classified as radio-selected AGNs or to be included in the sample of high-power radio sources (see Figures 2.2 and 2.3). However, many of the S-AGN galaxies contain a low-power radio source and/or an X-ray source. These nine objects are all represented on the G-M_{20} diagram shown in Figure 5.1(d) (five are also represented in panel (b) of that figure), and all are classified as being hosted by E/S0/Sa galaxies. Panel (d) of Figures 5.2 and 5.3 also include all nine galaxies, and on account of their concentrations the hosts are classified as early-type; however, two of the nine have Gini coefficients that edge them into the interacting region. It has also been found that the host galaxies of these AGNs are generally more asymmetric than the majority of the S-AGN galaxies. Combining the E/S0/Sa and early-type designations with the higher asymmetries suggests that these may be post-merger systems (Lotz et al. 2008b).

None of the optical spectra-selected AGNs hosted by interacting galaxies (as classified by G-M_{20} and/or C-A) have confirmed radio or X-ray emissions, but many of the X-ray-selected AGNs and high-power radio sources that are hosted by interacting galaxies (in particular, those so classified by G-M_{20}) also contain a radio source or an X-ray source, respectively. This is significant because it suggests an intrinsic difference between the optical spectra-selected AGNs and the X-ray-selected AGNs or high-power radio sources that are associated with interacting galaxies. Also, the interacting hosts of X-ray and radio AGNs/sources are found to have high values of G and M_{20} (and low values of A) when compared to the interacting hosts of optical spectra-selected AGNs, suggesting that the different AGN samples may be at different stages in their respective interactions (see Lotz et al. 2008b). Further exploration of this potential result and a discussion of the implications are presented in the next chapter.

The fraction of AGN host galaxies classified as interacting is roughly consistent with the fraction of control sample galaxies classified as interacting. However, the fraction of all galaxies (that meet necessary reliability criteria) at $0.2 < z < 1.2$ that are hosted by identified AGNs is quite small ($<$7%). These results indicate that (1) AGN host galaxies comprise an atypical sub-sample of the galaxies at $z \sim 1$, especially with respect to their stellar masses and colors, which has been shown before (e.g., Kauffmann et al. 2003), and (2) galaxy interactions do not invariably lead to significant nuclear activity. However, if the AGN host galaxies are compared to control samples that only include galaxies that have redshifts, $U - B$ colors, and B magnitudes similar to those of the AGN host galaxies (and for this exercise, not excluding the AGNs), then it is

found that the fraction of interacting galaxies that host an AGN is 18% (G-M_{20}) to 35% (C-A), significantly higher than the fraction determined above. This may offer support to the scenario in which mergers are expected to consistently lead to significant growth of a nuclear black hole, *if the galaxies involved have a certain set of characteristics.*

The authors of reports on such scenarios (e.g., Hopkins et al. 2008a,b) have made it is clear that there are qualifications placed on their scenario, such as the relative masses of the interacting objects. Mergers between galaxies of similar masses (major mergers), at least one of which harbors a quiescent black hole, are much more likely to result in a period of significant black hole growth than a merger between galaxies of very different masses (minor mergers). Although it is not currently possible to distinguish between major and minor mergers among the interacting galaxies in the samples described here, the fact that high-mass galaxies are much more likely than low-mass galaxies to host AGNs suggests that absolute galaxy mass may also be important in determining which galaxy interactions trigger an AGN.

Kinematically close galaxy pairs are neither more nor less frequently identified among any of the AGN samples as compared to the corresponding control samples. From this it can be concluded that either the black hole does not begin to accrete significantly until after the galaxies have merged, or else accretion-related AGN emission is heavily obscured by gas and dust in the galaxies during the interaction, and prior to coalescence.

Chapter 6

Color-Morphology Relationships of AGN Host Galaxies

6.1 Optical and UV-Optical Galaxy Colors

Baldry et al. (2004) analyzed the optical colors $(u - r)$ of a sample of low-redshift galaxies and found a bimodal distribution of red and blue galaxies that was well modeled by the sum of two Gaussians fitted to the individual red and blue galaxy distributions (see their Figures 3 and 4). Such results suggest a rapid decline in star formation, leading to an abrupt change in the predominant stellar ages and colors. However, Kennicutt (1998) explained that the ultraviolet continuum, to which young stars contribute significantly, provides a more accurate indicator of star formation rates. Following up on this, Wyder et al. (2007) examined the color-magnitude diagram of the UV-optical color $NUV - r$ for a sample of galaxies at $0.01 < z < 0.25$. Although Wyder

et al. (2007) found that Gaussians well modeled the *peaks* of the red and blue galaxy distributions, they found an excess of galaxies *between* the two peaks (see their Figures 12-14), in contrast to the results of Baldry et al. (2004) and supportive of a population of either star-forming galaxies slowly shutting down (likely located near the red edge of the blue sequence) or nearly quiescent galaxies with low levels of star formation, such as might be associated with a minor disturbance of an elliptical galaxy or a merger remnant (likely located near the blue edge of the red sequence). Wyder et al. (2007) also found that the UV-optical colors exhibit a wider separation between the red and blue sequences than the purely optical colors studied by Baldry et al. (2004), allowing a closer examination of the characteristics of the galaxies progressing from blue to red (or red to blue). Thus, UV-optical colors are particulary relevant for characterizing the host galaxies of the AGN samples discussed here and studying the possible connections between AGNs and galaxy interactions and between AGN feedback and the cessation of star formation.

As explained previously, the UV-optical colors are especially relevant to the current study. Unfortunately, the requirements for a reliable measurement of the $NUV-R$ color exclude 48% of the X-AGN galaxies and 67% of the R-AGN galaxies; the requirements also exclude ∼25% of the galaxies from each control sample and 8% of the S-AGN galaxies. The low level of exclusion for the S-AGN sample is due to the nature of the reliability requirement — a good fit between the optical spectrum and a spectral template — and the method of selection for this AGN sample, which out of necessity requires a reliable optical spectrum. No significant correlations have been

found between the exclusion of AGN host galaxies and X-ray luminosity, radio power, redshift, $U - B$ color, M_B, or the elliptical Petrosian radius. In order to maximize the number of galaxies described, an optical $(U - B)$ color-magnitude diagram (CMD; Figure 6.1) is presented first, followed by the UV-optical CMD (Figure 6.2).

The figures presented in this chapter consist of four panels, each presenting a sub-sample of AEGIS galaxies at $0.2 < z < 1.2$, following the same pattern as the figures presented in Chapter 5. Solid lines shown in the figures represent divisions between the color classifications defined in Chapter 2 and/or the morphology classifications defined in Chapter 3; the names of these classifications are shown in panel (a) of each figure. Symbols represent only those galaxies that meet the reliability criteria (see Chapters 2 and 3) for the specified color or morphology measurements, so the number of symbols in each panel may change between figures.

Panel (a) shows the most general sample possible that meets the relevant criteria for the measurements being presented. In panels (b)-(d), gray symbols represent galaxies in the control sample that corresponds to the AGN sample represented by the blue symbols. Symbols in panel (b) represent galaxies in the X-AGN and X-control samples, symbols in panel (c) represent galaxies in the R-AGN and R-control samples, and symbols in panel (d) represent galaxies in the S-AGN and S-control samples. For panels (b)-(d), 'x's represent either X-ray-selected AGNs [panel (b)] or X-ray sources ($L_{2-10\ \mathrm{keV}} > 10^{40}$ erg s^{-1}) [panels (c) & (d)], open squares represent high-power radio sources ($P_{1.4\ \mathrm{GHz}} > 10^{24}$ W Hz^{-1}), and 'S's represent optical spectra-selected AGNs. Filled diamonds represent sources that are high-power radio sources, X-ray sources, *and*

optical spectra-selected AGNs. An encircled symbol in panel (b) indicates that the AGN represented has an X-ray luminosity $L_{2-10\ \mathrm{keV}} > 10^{44}$ erg s^{-1}; in panel (c), circles mark radio-selected AGNs ($L_{1.4\ \mathrm{GHz}} > 10^{25}$ W Hz^{-1}).

6.1.1 Optical Colors of AGN Host Galaxies

Figure 6.1 shows the optical CMD of the three AGN samples and the corresponding control samples. Because the galaxies in the control samples were selected based in part on the similarity between their B magnitudes and optical colors to those comprising the AGN host galaxy samples, a strong correlation is found between the locations of the AGN samples on the CMD and the locations of the control samples. A series of K-S tests supports this quantitatively, giving probabilities 9% - 85% and 0.03% - 8% that the samples were drawn from the same parent population of $U-B$ colors and B magnitudes, respectively. In both cases, the X-AGN and X-control galaxies show the lowest probabilities, while the R-AGN and R-control galaxies show the highest probabilities.

Comparing panel (a) to panels (b)-(d) suggests that AGN host galaxies in general, and high-power radio sources in particular, are among the reddest and most luminous systems at the redshifts under consideration. Two exceptions are the optical spectra-selected AGNs hosted by blue galaxies, some of which approach the lower B magnitudes, and the optical colors of the X-AGN galaxies, which are only slightly more often red (45%) than blue (43%). For comparison, 73% of the R-AGN galaxies and 60% of the S-AGN galaxies are red. These fractions are summarized in Table 6.1.1.

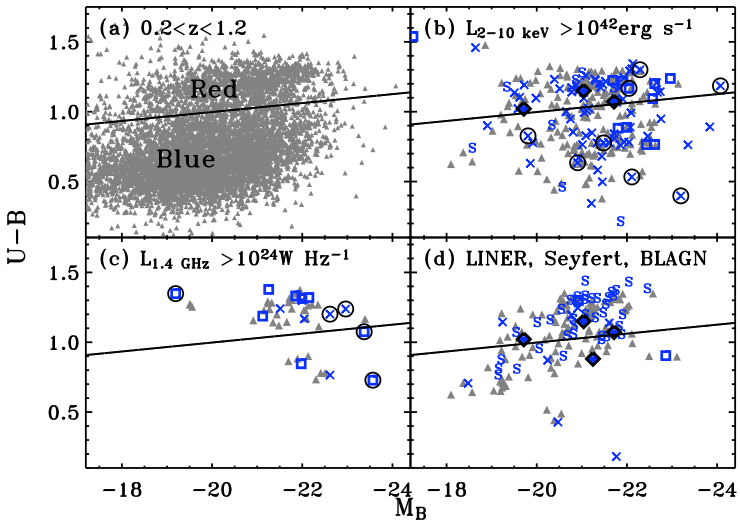

Figure 6.1: $U-B$ vs. M_B diagrams of the control and AGN samples *in the AEGIS*. Panels and symbols are as described in § 6.1.

Table 6.1: AGN host galaxy optical colors.

Sample	Sample Size	Red % (#)	Green % (#)	Blue % (#)	K-S %
X-AGN	93	45^{+8}_{-7} (42)	12^{+5}_{-4} (11)	43^{+8}_{-7} (40)	9
X-control	878	37±2 (324)	9±1 (80)	54±2 (474)	...
R-AGN	15	73^{+29}_{-22} (11)	7^{+15}_{-6} (1)	20^{+19}_{-11} (3)	85
R-control	77	78^{+11}_{-10} (60)	3^{+3}_{-2} (2)	19^{+6}_{-5} (15)	...
S-AGN	52	60^{+13}_{-11} (31)	15^{+8}_{-5} (8)	25^{+9}_{-7} (13)	24
S-control	516	52±3 (268)	13±2 (68)	35±3 (180)	...

The high fraction of red S-AGN galaxies is consistent with the method of selecting this AGN sample; the S-AGNs hosted by the two very blue galaxies ($U - B < 0.5$) are BLAGNs and X-ray-selected AGNs, but they are not radio sources (even at low radio powers). *HST*/ACS images reveal that both of these galaxies contain visible point sources which may affect the measured optical colors. The *HST*/ACS images of the two X-ray-selected AGNs hosted by the bluest galaxies that are *not* optical spectra-selected AGNs also suggest that the AGN may contribute significantly to the measured optical color; the third-bluest host (at $M_B \approx -21.5$) consists of a red elliptical with a significant patch of star formation, probably due to an interaction. The radio-selected AGN at $M_B \approx 19$ has a photometric redshift $z = 0.8$ and a significant radio flux; based on the *HST*/ACS image of the galaxy matched to this radio source, the host is a faint, red elliptical with a small region of possible star-formation just off one end.

6.1.2 UV-Optical Colors of AGN Host Galaxies

As discussed above, UV-optical colors exhibit an excess between the blue and red color classifications, suggesting that galaxies experience a transitionary period. Figure 6.2 provides the UV-optical CMD of the AGN and control samples. As with the optical colors, there are fairly high levels of correlation between the UV-optical colors of the AGN/high-power radio source host galaxies and the colors of the galaxies in the corresponding control samples, with probabilities 1% - 78% of having been drawn from the same parent population. The decrease in the number of galaxies in the samples, due to the requirements for the measurement of the $NUV - R$ colors, is very clear for the

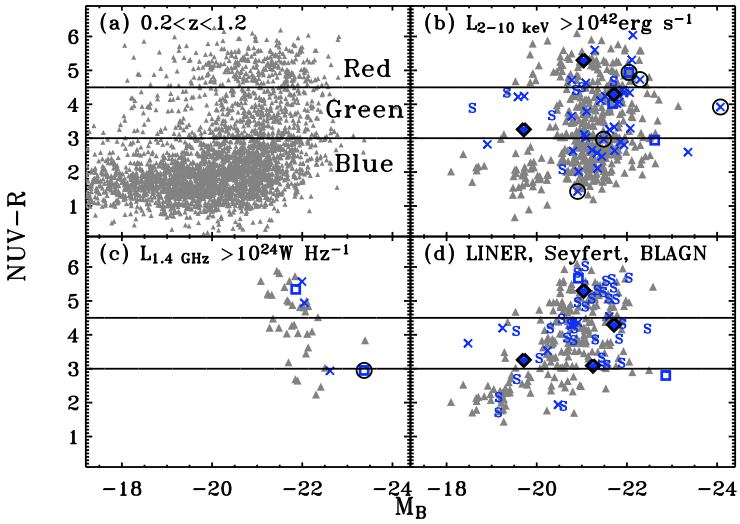

Figure 6.2: $NUV - R$ vs. M_B diagrams of the control and AGN samples *in the AEGIS*. Panels and symbols are as described in § 6.1.

radio sample, but the trends evident in Figure 6.2 are roughly the same as those seen on the optical CMD. In particular, the galaxies represented in panels (b) - (d) are still among the reddest and most luminous systems represented in panel (a).

Significant fractions of X-AGN (51%) and S-AGN (48%) galaxies are designated as "green valley" galaxies. These two AGN samples differ on the second most common color designation, with 31% of the X-AGNs hosted by blue galaxies and 35% of the S-AGNs hosted by red galaxies. With only five R-AGN galaxies, it is difficult to reach any statistically meaningful conclusions about that sample, but it does seem clear that they are rarely found in blue galaxies, and then only on the red edge of the blue cloud. Table 6.1.2 provides a summary of these numbers.

The fractions of optically blue AGN hosts that are in the UV-optical green

Table 6.2: AGN host galaxy UV-optical colors.

Sample	Sample Size	Red % (#)	Green % (#)	Blue % (#)	K-S %
X-AGN	49	18^{+8}_{-6} (9)	51^{+12}_{-10} (25)	31^{+10}_{-8} (15)	1
X-control	448	19±2 (86)	32±3 (143)	48±3 (217)	...
R-AGN	5	60^{+58}_{-33} (3)	0^{+37}_{-0} (0)	40^{+53}_{-26} (2)	78
R-control	36	50^{+15}_{-12} (18)	39^{+13}_{-10} (14)	11^{+9}_{-5} (4)	...
S-AGN	48	35^{+11}_{-9} (17)	48^{+12}_{-10} (23)	17^{+8}_{-6} (8)	44
S-control	227	32±4 (73)	44±4 (99)	24^{+4}_{-3} (55)	...

valley is consistent with the fraction of optically blue galaxies from the corresponding control samples in the UV-optical green valley; the same can be said for the optically red AGN hosts and the corresponding control samples. This supports the expectation that UV light from the AGNs does not strongly affect the $NUV - R$ colors for most AGN host galaxies (e.g., Kauffmann et al. 2007) and implies that most AGN hosts are in the green valley because of increased levels of star formation, relative to the levels of star formation going on in AGN hosts with red UV-optical colors.

6.2 AGN Host Galaxy Color-Morphology Relationships

Here we describe the color-morphology relationships of AGN host galaxies. Reliability criteria for the Sérsic profile measurements excluded 32% of the X-AGN galaxies, 12% of the X-control galaxies, 40% of the R-AGN galaxies, 18% of the R-control galaxies, 19% of the S-AGN galaxies, and 8% of the S-control galaxies. In order to discuss a more complete representation of AGN host galaxy Sérsic profiles, the Sérsic profiles are first shown with the *optical* colors of the AGN and control sample galaxies (Figure 6.3), and the *UV-optical* colors and the Sérsic profiles are presented (Figure 6.4).

6.2.1 $U - B$ Colors and Sérsic Profiles

The division between red and blue optical colors used by Willmer et al. (2006) is consistent with the horizontal line shown in each panel of Figure 6.3. Vertical lines separate the galaxies according to their dominant Sérsic profiles, as defined above. The decreased sample sizes do not affect the color trends seen in Figure 6.1 among AGN/high-luminosity radio source host galaxies and the corresponding control samples. However, the Sérsic profiles presented in Figure 6.3 indicate some disparity between the X-AGN and X-control galaxies and between the S-AGN and S-control galaxies, consistent with the low probabilities ($\leq$0.4%) that the Sérsic profiles of these AGN and control samples were drawn from the same parent populations. The high-power radio sources have Sérsic profiles that seem quite consistent with the radio control sample profiles, but the small sample size necessitates a high level of caution regarding significant conclusions.

Table 6.2.1 summarizes the fractions and numbers of AGN and control galaxies categorized as bulge-dominated, ambiguous, or disk-dominated (following the definitions from § 3.2. Galaxies in the X-AGN sample are most often classified as bulge-dominated (68%), with statistically consistent fractions classified as disk-dominated (19%) and ambiguous (13%). Galaxies in the X-control sample, however, are more often classified as disk-dominated (49%) and less often classified as bulge-dominated (36%).

What really stands out is a difference in color distribution as a function of the Sérsic index. The blue galaxies in the X-control sample are very likely to have

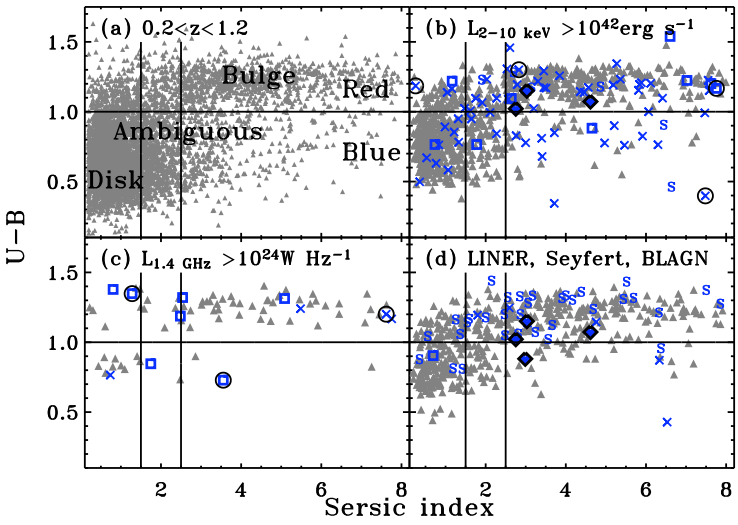

Figure 6.3: $U-B$ diagrams of the control and AGN samples *in the AEGIS*. Panels and symbols are as described in § 6.1.

Table 6.3: AGN host galaxy Sérsic profiles.

Sample	Sample Size	Disk-dominated % (#)	Ambiguous % (#)	Bulge-dominated % (#)	K-S %
X-AGN	78	19^{+6}_{-5} (15)	13^{+5}_{-4} (10)	68^{+11}_{-9} (53)	3e-5
X-control	782	49±3 (384)	15±1 (114)	36±2 (280)	...
R-AGN	11	27^{+27}_{-15} (3)	18^{+24}_{-12} (2)	55^{+33}_{-22} (6)	74
R-control	66	23^{+8}_{-6} (15)	9^{+5}_{-4} (6)	68^{+12}_{-10} (45)	...
S-AGN	44	20^{+9}_{-7} (9)	14^{+8}_{-5} (6)	66^{+15}_{-12} (29)	0.4
S-control	466	40±3 (185)	$16^{\pm}2$ (75)	44±3 (204)	...

disk-dominated profiles, while there are roughly equal numbers of blue X-AGN host galaxies classified as disk-dominated and as bulge-dominated. Furthermore, although the bulge-dominated galaxies in the X-control sample are almost exclusively red, there are almost as many blue galaxies among the bulge-dominated X-AGN host galaxies as there are red galaxies. There are clearly at least three possibile explanations for this result. (1) The AGNs significantly contribute to the measured colors of their host galaxies, leading to artificially low $U - B$ colors of bulge-dominated galaxies; (2) the AGNs strongly affect the measurement of the Sérsic profiles, artificially increasing the Sérsic indices of AGN hosts with disk-dominated profiles; or (3) bulge-dominated AGN host galaxies are undergoing higher levels of star formation than a comparable sample of bulge-dominated galaxies that do not host AGNs. Options (1) and (2) are of particular concern for objects such as the AGN host with low optical color, high Sérsic index, and high X-ray luminosity. Based on the discussion of Figure 6.2, option (1) does not seem to pose a significant problem, except in the case of very luminous, unobscured AGNs, such as are found in hosts with $U - B < 0.5$. Option (3) will be further discussed along with the comparison between the UV-optical colors and the Sérsic profiles.

Figure 6.3(c) presents the optical colors and Sérsic profiles of the radio samples. As for the X-ray samples, it is reassuring to find that the distribution of optical colors of the R-AGN and R-control galaxies are very similar, further supported by a 78% probability that the two samples were drawn from the same parent population (based on a K-S test). In contrast to the X-ray samples, but subject to concerns about small number statistics, the two samples shown in Figure 6.3(c) have very similar Sérsic

profiles, consistent with a 74% probability that they were drawn from the same parent population. Both samples are most heavily represented in the bulge-dominated category (R-AGN: 55%; R-control: 68%), with 27% and 23% of the R-AGN and R-control galaxies, respectively, classified as disk-dominated. Most R-AGN galaxies follow the color-morphology trends exhibited by the R-control galaxies, with blue (red) galaxy colors corresponding to small (large) Sérsic indices. A notable exception is the AGN with blue galaxy colors and Sérsic index ~ 3.5, which could be explained by one or more of the three possibilities listed above. Examination of the ACS image reveals that this elliptical galaxy is undergoing probable interaction-related star formation.

The match between the optical colors of S-AGN and S-control galaxies is also strong, with a 44% probability of having been drawn from the same parent population. This is easily explained by the color requirement used in the AGN selection process; most S-AGN galaxies have optical colors $U - B > 0.8$, so the majority of the control sample is naturally limited by a similar requirement, with a few exceptions for control sample galaxies with properties matched to broad-line AGNs. As presented in Figure 6.3(d) and Table 6.2.1, the colors of S-AGN and S-control galaxies have only a 0.4% probability of having been drawn from the same parent population. However, if we exclude the contribution from AGN hosts and control sample galaxies with colors bluer than $U-B = 0.8$, then the probability increases to 7%.

Regardless of color, the S-AGN galaxies are most often classified as bulge-dominated (66%) and least often classified as disk-dominated (20%). The control sample galaxies follow the same trend, but the significance of the results depends strongly on

whether or not we include the subset of control sample galaxies with $U-B < 0.8$. If these bluer galaxies are included, the fraction of bulge-dominated galaxies (44%) is higher, but it is statistically consistent with the fraction of disk-dominated galaxies (40%). Without the bluer control sample galaxies, the fraction of bulge-dominated galaxies (53%) is significantly higher than the fraction of disk-dominated galaxies (30%), and this may be a more reasonable comparison, given the rarity of broad-line AGNs in the S-AGN sample and the possibility that measurements of such systems may be subject to contamination from the AGN, as discussed above.

6.2.2 $NUV - R$ Colors and Sérsic Profiles

The final figure to be discussed in this section, Figure 6.4, compares the Sérsic indices of the AGN and control galaxies to their UV-optical colors. As mentioned previously, the criteria required for reliable measurements of the Sérsic index and the UV-optical colors each exclude a sometimes significant fraction of the control and AGN samples; together, the two sets of criteria exclude between 21% (S-AGNs) and 65% (R-AGNs) of the AGN samples. The R-AGN sample now contains only two galaxies, both of which are also X-ray-selected AGNs, so although these objects are presented in panel (c) of Figure 6.4, the results are not discussed. No correlations have been found between exclusion by the Sérsic reliability criteria and the redshift, $U - B$ color, radio power, or X-ray luminosity of AGN host galaxies.

There is a significant lack of red ($NUV - R > 4.5$), disk-dominated galaxies in Figure 6.4, contrasting the results shown by Figure 6.3. Instead, most of the disk-

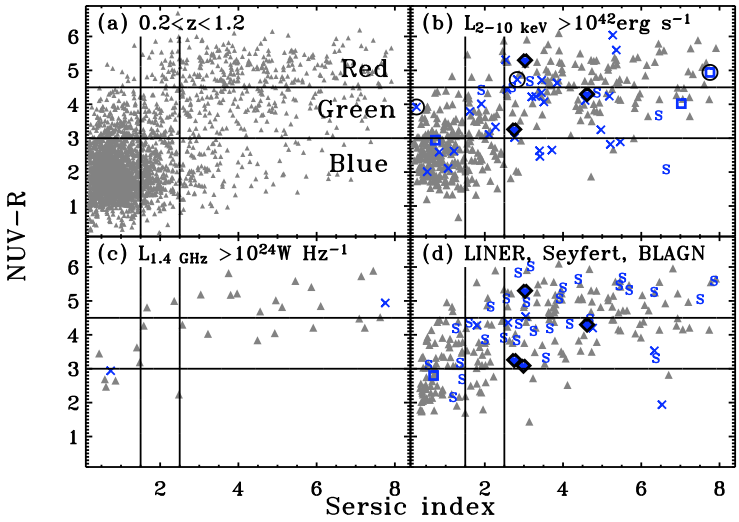

Figure 6.4: $NUV - R$ vs. Sérsic indices of the control and AGN samples *in the AEGIS*. Panels and symbols are as described in § 6.1.

dominated galaxies that have red *optical* colors have green or even blue *UV-optical* colors, supporting the expectation that the UV-optical colors are more sensitive to subtle differences hidden by the purely optical colors. Additional support for this increased sensitivity comes from a comparison between the optical and the UV-optical colors of the galaxies represented by diamonds in panels (b) and (d) of Figures 6.3 and 6.4. In Figure 6.3, the locations of the symbols suggest that the galaxies have similar optical colors, but the UV-optical colors indicated in Figure 6.4 reveal significant differences among the current star-formation rates of these galaxies. There is also a difference between the appearance of the optical red sequence and the UV-optical red sequence; the latter covers a significantly wider range of color and a narrower range of Sérsic indices.

Most disk-dominated X-AGN galaxies have blue UV-optical colors, and the remaining disk-dominated X-AGN galaxies are in the UV-optical green valley. Approximately half of the X-AGNs hosted by bulge-dominated galaxies are in the green valley, and the remainder are located on the red sequence at only a slightly higher rate than in the blue cloud. However, the majority of the bulge-dominated galaxies in the X-control sample are on the red sequence or at the red edge of the green valley; in fact, there seems to be a general dearth of bulge-dominated, X-AGN galaxies through the middle of the green valley.

Two of the most X-ray-luminous AGNs represented in Figure 6.4(b) have hosts designated as red, bulge-dominated galaxies; these designations are verified by the *HST*/ACS images. The third very X-ray luminous AGN has a green, disk-dominated host galaxy, as determined by color and morphology measurements; the *HST*/ACS image reveals a highly disturbed galaxy with scattered regions of possible star formation and a prominent point source. Examples such as these strongly support the reliability of the measured Sérsic profiles and $NUV - R$ colors.

Galaxies hosting optical spectra-selected AGNs generally follow the color-morphology patterns set by the control sample, with the exception of the BLAGNs. The disk-dominated hosts of optical spectra-selected AGNs are blue and green at approximately the same rate. Bulge-dominated hosts of optical spectra-selected AGNs are identified as red about as often as green, with a minimal fraction classified as blue. As with the bulge-dominated hosts of X-ray-selected AGNs, the bulge-dominated hosts of optical spectra-selected AGNs are typically absent from the middle of the UV-optical

green valley.

6.3 Discussion

The host galaxies of X-ray and optical spectra-selected AGNs are roughly evenly split between red and green $NUV - R$ colors (cf. Figure 6.1). If the green valley truly represents a transition region from a period of significant star formation to a period of relative quiescence, then Figure 6.4 suggests that a significant fraction of AGNs are hosted by galaxies undergoing this transition between high and low levels of star formation. Although the direction of this transition is not entirely obvious, the bulge-dominated profiles of many of the AGN host galaxies strongly suggest that they are remnants of recent galaxy mergers. The interaction between the galaxies involved would have significantly increased the star-formation in the galaxies, while also contributing to significant growth of the black hole.

At the time of observation, the galaxies have merged and morphologically settled to ellipticals, with occasional evidence remaining of the recent interaction. However, their UV-optical colors indicate higher levels of star formation than is expected from elliptical galaxies; for example, at similar Sérsic indices, X-control galaxies tend to have relatively redder colors than the X-AGN galaxies. The relative paucity of bulge-dominated X-AGN galaxies in the middle of the green valley (consistent with results from Martin et al. 2007) suggests a rapid decrease in the star-formation rates of these galaxies, possibly caused by feedback from the AGN.

Chapter 7

Conclusion

7.1 Summary

The morphologies of AGN host galaxies have been investigated using morphology and color measurements of simulations and multi-wavelength observations. Simulations suggest that the color and morphology measurements are generally reliable for low-luminosity AGNs, but may become severely contaminated by AGNs contributing 20% or more of the B-band flux. However, many of these AGNs would also be identifiable as containing a visible point source, so that the results could be flagged as needing extra investigation.

Morphologies suggest that AGN host galaxies *are* more likely than galaxies in a carefully selected control sample to be identified as interacting, but this is not the case with kinematic close pair identifications; this may restrict the time during which the AGN is likely to turn on. AGN host galaxies are also generally more likely to be

classified as bulge-dominated (or early-type or E/S0/Sa) than the control sample. This confirms previous work with X-ray-selected AGNs, and extends it to high-power radio sources and optical spectra-selected AGNs. AGN host galaxy UV-optical colors tend to be redder than the colors of the control sample galaxies, and there is a strong possibility that the presence of some of the AGN hosts in the green valley is somehow caused by some form of feedback from the AGN.

7.2 Suggested future work

7.2.1 Stacking X-ray and Radio Images

Models based on merging galaxy simulations (e.g., Hopkins et al. 2008a,b) advocate violent AGN feedback and predict Compton-thick obscuration of AGNs, beginning when the AGNs are triggered during an interaction and lasting until the original galaxies have fully merged. If this model is accurate, then the true fraction of AGNs hosted by interacting galaxies may be significantly higher than the fraction directly detected with current X-ray and/or radio observations. A more careful investigatation of this prediction might include a search for populations of obscured AGNs by stacking X-ray and/or radio images, after excluding the 5-σ detections; this work is already underway using the X-ray images. For example, Georgakakis et al. (2008) stacked the X-ray images of galaxy samples defined by their optical colors and found that gas accretion onto a nuclear black hole may last longer than star formation in the stellar spheroid.

Another study, still in progress, involves the separation of galaxies into *morphologically* defined samples. Currently, early-type and late-type galaxies are sub-divided into red and blue samples (based on the optical colors), and merging galaxies are sub-divided into early-stage mergers and late-stage mergers (following Lotz et al. 2008b). If late-stage mergers are found to be more likely than early-stage mergers to host obscured AGNs, this would tentatively support the models by suggesting that (1) AGNs are triggered *during* the interaction, because they are more prevalent among mergers in the later stages of interactions, and (2) mergers may commonly host obscured AGNs. The 1.8 Ms (total) of additional *Chandra* time for the AEGIS is expected to provide more conclusive results. Radio images are also available to conduct a similar study in search of radio-obscured AGNs.

7.2.2 Higher-redshift analyses

Paralleling the current work at $z \sim 1$, it would also be educational to study AGNs at $z \sim 2$. Using the soon-to-be-installed *HST*/Wide Field Camera 3 (WF3)[1], it should be possible to morphologically identify mergers, etc., at higher redshifts than allowed by current instruments and techniques. Investigation of a higher redshift AGN population will provide insight into very early stages of AGNs and stellar spheroids, helping researchers to better understand the history of the Universe.

[1] http://www.stsci.edu/hst/wfc3

7.2.3 "Observing" Simulated Galaxy Mergers Involving AGNs

To improve our understanding of how well observations support or contradict current models, we need to know what results the simulations would provide under the same scrutiny applied to the observations. To this end, it would be instructive to perform morphological analyses, paralleling the work presented here, using images from galaxy merger simulations. It would be particularly useful to determine the observable properties (e.g., morphology, X-ray luminosity) at various stages during the interactions and during the lifetimes of the AGNs, and then determine what observations might be expected in fields such as the AEGIS and GOODS-N.

These measurements will be particularly useful because the models make specific predictions about the bolometric luminosities of the AGNs at various times during the interactions, and in order to properly compare such predictions to observational results, we need to know the measured morphologies of the galaxies during the interaction stages for which the AGNs have the specified luminosities. It will also be useful to measure the radio luminosities of the AGNs during the simulated interactions to facilitate comparisons between the models and the results presented here. Following the parallel analyses of observations and simulations, a natural final step would be a thorough comparison between the two sets of results in order to determine the accuracy of the models and strengthen our understanding of current and future observations and simulations.

7.2.4 Investigating the relationship between M_{BH} and $M_{spheroid}$

The research presented here focused heavily on the relationship between galaxy interactions and AGNs, with a more cursory focus on the evolution of the associated stellar spheroids. A logical continuation of this research would be a more complete investigatation of the astrophysical processes that cause the observed correlation between a galaxy's black hole mass (M_{BH}) and its stellar spheroid mass ($M_{spheroid}$). One possible line of research could begin with additional analyses of two sets of current simulations — those associated with violent AGN feedback models and those associated with non-violent AGN feedback models — by tracking the evolution of a stellar spheroid throughout an interaction and the AGN stages. Using these "observations", one could then simultaneously measure the black hole mass and the stellar spheroid mass, determine any time-dependent relationship between the two, and establish which of the two initiates and halts the growth cycle, according to each set of simulations.

The resulting predictions could then be tested by analyzing observations of AGN hosts and/or spheroid-dominated galaxies, depending on the outcome of the simulation analysis. Potential results include (1) indications that black hole growth and stellar spheroid growth last for approximately the same amount of time, but that these periods of growth are offset in time (e.g., black hole growth begins before stellar spheroid growth begins and then ends before stellar spheroid growth ends, or vice versa); (2) a situation in which the black hole and the stellar spheroid experience alternating growth spurts; or (3) a system in which the black hole (or stellar spheroid) is the first to begin

and the last to end its growth cycle. In order for each of these situations to remain consistent with observed mass relationships, the amount of time that passes between the beginning or ending of the spheroid and black hole growth must be relatively short so that neither the stellar spheroid mass nor the black hole mass experiences a significant deviation from the M_{BH}-σ relation; the time resolution of recent simulations should be sufficient to make the necessary distinction.

The numerous surveys already available, such as the GOODS-N and the AEGIS, will serve as a starting point for testing the results suggested by the simulations, but it will undoubtedly be necessary to complete new observations specifically designed to support (or contradict) predictions. For instance, if the results indicate a series of alternating growth spurts, one might want to study two samples of star-forming galaxies which have significant bulges — one composed of galaxies having similar stellar spheroid masses and the other composed of galaxies having similar black hole masses. One would then carefully measure the corresponding black hole and stellar spheroid masses of the two samples, along with the ages of the stellar spheroids. A correlation between scatter about the established M_{BH}-σ relationship and the ages of the stellar spheroids, at a given redshift, may support hypothetical predictions, although it would also raise more questions, such as why the growth of the black hole and the stellar spheroid seemingly take turns following each other on a rather short timescale.

This proposed research builds upon current research by looking at stellar spheroid evolution from a different perspective. While the work presented here examined the potential causes and effects of the growth, the proposed research may allow

a determination of the pattern of growth by tracking the development of both the black hole and the stellar spheroid using simulations and observations. The predicted rapid decline of stellar spheroid growth due to AGN feedback suggests a reason for the observed galaxy color bimodality — as the stars age, there will be a net change from young, blue stars to old red stars. The results obtained by investigating stellar spheroid evolution will address the galaxy color bimodality and help us to better understand how and why galaxies evolve as observed.

Bibliography

Abraham, R. G., van den Bergh, S., & Nair, P. 2003, *ApJ*, **588**, 218

Alexander, D. M., Aussel, H., Bauer, F. E., Brandt, W. N., Hornschemeier, A. E., Vignali, C., Garmire, G. P., & Schneider, D. P. 2002, *ApJ*, **568**, L85

Alexander, D. M., et al. 2003, *AJ*, **126**, 539

Alonso-Herrero, A., et al. 2004, *ApJS*, **154**, 155

Antonucci, R. R. J. & Miller, J. S. 1985, *ApJ*, **297**, 621

Baldry, I. K., Glazebrook, K., Brinkmann, J., Ivezić, Z., Lupton, R. H., Nichol, R. C., & Szalay, A. S. 2004, *ApJ*, **600**, 681

Balogh, M. L., Baldry, I. K., Nichol, R., Miller, C., Bower, R., & Glazebrook, K. 2004, *ApJ*, **615**, L101

Barger, A. J., Cowie, L. L., Mushotzky, R. F., Yang, Y., Wang, W.-H., Steffen, A. T., & Capak, P. 2005, *AJ*, **129**, 578

Barger, A. J., Cowie, L. L., & Wang, W.-H. 2007, *ApJ*, **654**, 764

Barger, A. J., et al. 2003, *AJ*, **126**, 632

Barbmy, P., et al. 2006, *ApJ*, **642**, 126

Barmby, P., Huang, J.-S., Ashby, M. L. N., Eisenhardt, P. R. M., Fazio, G. G., Willner, S. P., & Wright, E. L. 2008, *ApJS*, **177**, 431

Beck-Winchatz, B. & Anderson, S. F. *AJ*, **117**, 2582

Bell, E. F., Phleps, S., Somerville, R. S., Wolf, C., Borch, A., & Meisenheimer, K. 2006a, *ApJ*, **652**, 270

Bell, E. F., et al. 2004a, *ApJ*, **600**, L11

—. 2006b, *ApJ*, **640**, 241

—. 2004b, *ApJ*, **608**, 752

Bennert, N., Canalizo, G., Jungwiert, B., Stockton, A., Schweizer, F., Peng, C. Y., & Lacy, M., 2008, *ApJ*, **677**, 846

Bertin, E. & Arnouts, S. 1996, *A&AS*, **117**, 393

Biggs, A. D. & Ivison, R. J. 2006, *MNRAS*, **371**, 963

Birnboim, Y., Dekel, A., & Neistein, E. 2007, *MNRAS*, **380**, 339

Blanton, M. R. 2006, *ApJ*, **648**, 268

Blanton, M. R., et al. 2003, *ApJ*, **594**, 186

Brandt, W. N., et al. 2001, *AJ*, **122**, 2810

Brown, M. J. I., Dey, A., Jannuzi, B. T., Brand, K., Benson, A. J., Brodwin, M., Croton, D. J., & Eisenhardt, P. R. 2007, *ApJ*, **654**, 858

Bruzual, G., & Charlot, S. 2003, *MNRAS*, **344**, 1000

Bundy, K., Ellis, R. S., & Conselice, C. J. 2005, *ApJ*, **625**, 621

Bundy, K., et al. 2006, *ApJ*, **651**, 120

—. 2008, *ApJ*, **681**, 931

Capak, P., et al. 2004, *AJ*, **127**, 180

Chabrier, G. 2003, *PASP*, **115**, 763

Ciliegi, P., et al. 2003, *A&A*, **398**, 901

Ciliegi, P., Zamorani, G., Hasinger, G., Lehmann, I., Szokoly, G., & Wilson, G. 2005, *A&A*, **441**, 879

Ciotti, L. & Ostriker, J. P. 2007, *ApJ*, **665**, 1038

Cirasuolo, M., et al. 2007, *MNRAS*, **380**, 585

Coe, D, Benitez, N., Sanchez, S. F., Jee, M., Bouwens, R., & Ford, H. 2006, *AJ*, **132**, 926

Coil, A. L., Newman, J. A., Kaiser, N., Davis, M., Ma, C.-P., Kocevski, D. D., & Koo, D. C. 2004, *ApJ*, **617**, 765

Condon, J. J. 1992, *ARA&A*, **30**, 575

Conselice, C. J. 2003, *ApJS*, **147**, 1

Conselice, C. J., et al. 2007, *ApJ*, **660**, L55

Cox, T. J., Jonsson, P., Primack, J. R., & Somerville, R. 2006, *MNRAS*, **373**, 1013

Croton, D. J., et al. 2006, *MNRAS*, **365**, 11

Cuillandre, J.-C., Luppino, G., Starr, B., & Isani, S. 2001, in *Proc. Semaine de l'Astrophysique Francaise*, eds. F. Combes, D. Barret, & F. Thévenin (Les Ulis: EdP-Sciences), 605

Davis, M., et al. 2003, *Proc. SPIE*, **4834**, 161

—. 2007, *ApJ*, **660**, L1

de Vaucouleurs, G. 1961, *ApJS*, **5**, 233

Di Matteo, T., Springel, V., & Hernquist, L. 2005, *Nature*, **433**, 604

—. 2007, *ApJ*, **660**, L1

Donley, J. L., Rieke, G. H., Rigby, J. R., & Pérez-González, P. G. 2005, *ApJ*, **634**, 169

Faber, S. M., et al. 2003, *Proc. SPIE*, **4841**, 1657

Faber, S. M., et al. 2007, *ApJS*, **665**, 265

Fang, T., et al. 2007, *ApJ*, **660**, L27

Fasano, G. & Franceschini, A. 1987, *MNRAS*, **225**, 155

Ferguson, H. C., Dickinson, M., Williams, R. 2000, *ARA&A*, **38**, 667

Ferrarese, L. & Merritt, D. 2000, *ApJ*, **539**, L9

Flores, H., et al. 1999, *ApJ*, **517**, 148

Fomalont, E. B., Windhorst, R. A., Kristian, J. A., & Kellerman, K. I. 1991, *AJ*, **102**, 1258

Francis, P. J., Hewett, P. C., Foltz, C. B., Chaffee, F. H., Weymann, R. J., & Morris, S. L. 1991, *ApJ*, **373**, 465

Gebhardt, K., et al. 2000, *ApJ*, **539**, L13

Gehrels, N. 1986, *ApJ*, **303**, 336

Georgakakis, A., et al. 2006, *MNRAS*, **371**, 221

—. 2008, *MNRAS*, **385**, 2049

Gerke, B. F., et al. 2007, *ApJ*, **660**, L23

Giavalisco, M., et al. 2004, *ApJ*, **600**, L93

Gilliland, R. L., & Riess, A. G. 2002, *HSTC.Conf*, 61

Griffith, R. 2009, "The Advanced Camera for Surveys General Catalogue ACS-GC: A Galaxy Catalog at High Redshift", in preparation

Grogin, N. A., et al. 2005, *ApJ*, **627**, L97

—. 2003, *ApJ*, **595**, 685

Haarsma, D. B., Partridge, R. B., Windhorst, R. A., & Richards, E. A. 2000, *ApJ*, **544**, 641

Häussler, B., et al. 2007, *ApJS*, **172**, 615

Hodapp, K.-W., et al. 1996, *New Astronomy*, **1**, 177

Hopkins, P. F., Cox, T. J., Kereš, D., & Hernquist, L. 2008a, *ApJS*, **175**, 390

Hopkins, P. F., Hernquist, L., Cox, T. J., Di Matteo, T., Martini, P., Robertsons., B., & Springel, V. 2005a, *ApJ*, **630**, 705

Hopkins, P. F., Hernquist, L., Cox, T. J., & Kereš, D. 2008b, *ApJS*, **175**, 356

Hopkins, P. F., Hernquist, L., Martini, P., Cox, T. J., Roberston, B., Di Matteo, T., & Springel, V. 2005b, *ApJ*, **625**, L71

Ilbert, O., et al. 2006, *A&A*, **457**, 841

Ivison, R. J., et al. 2007, *ApJ*, **660**, L77

Jacoby, G. H., Liang, M., Vaughnn, D., Reed, R., & Armandroff, T. 1998, *Proc. SPIE*, **3355**, 721

Kauffmann, G. & Haenelt, M. 2000, *MNRAS*, **311**, 576

Kauffmann, G., et al. 2007, *ApJS*, **173**, 357

—. 2003, *MNRAS*, **346**, 1055

Kennicutt, R. C. 1998, *ARA&A*, **36**, 189

Kinney, A. L., Calzetti, D., Bohlin, R. C., McQuade, K., Storchi-Bergmann, T., & Schmitt, H. R. 1996, *ApJ*, **467**, 38

Kormendy, J. & Richstone, D. 1995, *ARA&A*, **33**, 581

Krist, J. 1993, *ASPC*, **52**, 536

Laird, E. S., Nandra, K., Adelberger, K. L., Steidel, C. C., & Reddy, N. A. 2005, *MNRAS*, **359**, 47

Laird, E. S., et al. 2008, *ApJS*, in press, arXiv:0809.1349

Le Floc'h, E. et al. 2007, *ApJ*, **660**, L65

Lehnert, M. D., et al. 1999, *ApJS*, **123**, 351

Li, C., Kauffmann, G., Heckman, T. M., Jing, Y. P., & White, S. D. M., 2008a, *MNRAS*, *385*, 1903

Li, C., Kauffmann, G., Heckman, T. M., White, S. D. M., & Jing, Y. P., 2008b, *MNRAS*, *385*, 1915

Lilly, S. J., Le Fevre, O., Crampton, D., Hammer, F., & Tresse, L. 1995, *ApJ*, **455**, 50

Lin, L., et al. 2007, *ApJ*, **660**, L51

—. 2004, *ApJ*, **617**, L9

Lotz, J. M., et al. 2008a, *ApJ*, **672**, 177

Lotz, J. M., Jonsson, P., Cox, T. J., & Primack, J. R. 2008b, *MNRAS* submitted, arXiv:0805.1246

Lotz, J. M., Primack, J., & Madau, P. 2004, *AJ*, **128**, 163 (LPM04)

Magorrian, J., et al. 1998, *AJ*, **115**, 2285

Martin, D. C., et al. 2005, *ApJ*, **619**, L1

—. 2007, *ApJS*, **173**, 342

McQuade, K., Calzetti, D., & Kinney, A. L. 1995, *ApJS*, **97**, 331

Mihos, J. C. & Hernquist, L. 1996, *ApJ*, **464**, 641

Miyaji, T., Sarajedini, V., Griffiths, R. E., Yamada, T., Schurch, M., Cristóbal-Hornillos, D., & Motohara, K. 2004, *AJ*, **127**, 3180

Miyazaki, S., et al. 2002, *PASJ*, **54**, 833

Montero-Dorta, A. D., et al. 2008, *MNRAS* submitted, arXiv:0801.2769

Moore, B., Lake, G., & Katz, N. 1998, *ApJ*, **495**, 139

Morrissey, P., et al. 2007, *ApJS*, **173**, 682

—. 2005, *ApJ*, **619**, 7

Moustakas, L. A., et al. 2007, *ApJ*, **660**, L31

Muller, G. P., Reed, R., Armandroff, T., Boroson, T. A., Jacoby, G. H. 1998, *Proc. SPIE*, **3355**, 577

Murray, S. S., et al. 2005, *ApJS*, **161**, 1

Nandra, K., et al. *ApJ*, **660**, L11

—. *MNRAS*, **356**, 568

Noeske, K. G., et al. 2007, *ApJ*, **660**, L47

O'Dowd, M., Urry, C. M., & Scarpa, R. 2002, *ApJ*, **580**, 96

Osterbrock, D. E. 1978, *Proc. Nat. Acad. Sci. USA*, **75**, 540

Osterbrock, D. E. 1981, *ApJ*, **249**, 462

Park, S. Q., et al. 2008, *ApJ*, **678**, 744

Patton, D. R., et al. 2002, *ApJ*, **565**, 208

Peng, C. Y., Ho, L. C., Impey, C. D., & Rix, H. 2002, *AJ*, **124**, 266

Peterson, B. M. 1997, *An Introduction to Active Galactic Nuclei* (Cambridge: Cam-

bridge University Press)

Pierce, C. M., et al. 2007, *ApJ*, **660**, L19

Richards, E. A. 2000, *ApJ*, **533**, 611

Salim, S., et al. 2005, *ApJ*, **619**, L39

—. 2007, *ApJS*, **173**, 267

Sarajedini, V., et al. 2006, *ApJS*, **166**, 69

Scarlata, C., et al. 2007, *ApJS*, **172**, 494

Schawinski, K., Thomas, D., Sarzi, M., Maraston, C., Kaviraj, S., Joo, S.-J., Yi, S. K., & Silk, J. 2007, *MNRAS*, **382**, 1415

Schweizer, F., Seitzer, P., Faber, S. M., Burstein, D., Dalle Ore, C. M., Gonzalez, J. J., 1990, *ApJ*, **364**, 33

Seymour, N., et al. 2008, *MNRAS*, **386**, 1695

Simmons, B. D. & Urry, C. M. 2008, *ApJ*, **683**, 644

Somerville, R. S., Hopkins, P. F., Cox, T. J., Robertson, B. E., & Hernquist, L. 2008, *MNRAS*, **391**, 481

Springel, V., Di Matteo, T., & Hernquist, L., 2005, *ApJ*, **620**, 79

Strateva, I., et al. 2001, *AJ*, **122**, 1861

Teng, S., et al. 2005, *ApJ*, **633**, 664

Thompson, T. A., Quataert, E., Waxman, E., Murray, N., & Martin, C. L. 2006, *ApJ*, **645**, 186

Tran, H. D., Miller, J. S., & Kay, L. E. 1992, *ApJ*, **397**, 452

Urrutia, T., Lacy, M., & Becker, R. H., 2008, *ApJ*, **674**, 80

Urry, C. M., Falomo, R., Scarpa, R., Pesce, J. E., Treves, A., & Giavalisco, M. 1999, *ApJ*, **512**, 88

van Dokkum, P. G. 2005, *AJ*, **130**, 2647

Weiner, B. J., et al. 2005, *ApJ*, **620**, 595

Williams, R. E., et al. 1996, *AJ*, **112**, 1335

Willmer, C. N. A., et al. 2006, *ApJ*, **647**, 853

Willner, S. P., et al. 2006, *AJ*, **132**, 2159

Wilson, G., et al. 2007, *ApJ*, **660**, L59

Wirth, G. D., et al. 2004, *AJ*, **127**, 3121

Wolfe, T., Reed, R., Blouke, M. M., Boroson, T. A., Armandroff, T., Jacoby, G. H. 1998, *Proc. SPIE*, **3355**, 487

Wyder, T. K., et al. 2007, *ApJS*, **173**, 293

Yan, R., Newman, J. A., Faber, S. M., Konidaris, N., Koo, D., & Davis, M. 2006, *ApJ*, **648**, 281